Received: 6 September 2024 | Revised: 13 March 2025 | Accepted: 17 March 2025

DOI: 10.1002/qj.4986

Quarterly Journal of the Royal Meteorological Society RMetS

RESEARCH ARTICLE

Sensitivities of warm conveyor belt ascent, associated precipitation characteristics and large-scale flow pattern: Insights from a perturbed parameter ensemble

Annika Oertel[1] | **Annette K. Miltenberger**[2] | **Christian M. Grams**[1,3] | **Corinna Hoose**[1]

[1]Institute for Meteorology and Climate Research Troposphere Research (IMKTRO), Karlsruhe Institute of Technology, Karlsruhe, Germany

[2]Institute for Atmospheric Physics, Johannes Gutenberg University, Mainz, Germany

[3]Federal Office of Meteorology and Climatology, MeteoSwiss, Zurich-Airport, Switzerland

Correspondence
Annika Oertel, Institute for Meteorology and Climate Research Troposphere Research (IMKTRO), Karlsruhe Institute of Technology, Karlsruhe, 76131, Germany.
Email: annika.oertel@kit.edu

Funding information
Deutsche Forschungsgemeinschaft, Grant/Award Number: SFB/TRR 165; Helmholtz Association, Grant/Award Number: VH-NG-1243; Italia-Deutschland science-4-services network in weather and climate (IDEA-S4S), Grant/Award Number: 4823IDEAP6

Abstract

The characteristic and strongly precipitating cloud band near extratropical cyclones is associated with a coherent cross-isentropically ascending airstream, the warm conveyor belt (WCB). The WCB ascent characteristics and associated diabatic heating are influenced by cloud microphysical processes and environmental conditions in the WCB inflow region. The former relies on the cloud microphysical parametrisation, and the latter on initial and/or boundary conditions of thermodynamic variables. Altogether, this introduces uncertainty in numerical weather prediction (NWP) forecasts of the WCB characteristics and ultimately the prediction of the large-scale midlatitude flow. We quantify the relative influence of perturbations on various cloud microphysical processes and WCB inflow temperature and moisture (via modification of sea-surface temperature) for a case study and thereby focus on uncertainty in WCB ascent behaviour, associated precipitation characteristics, and properties of the amplifying ridge downstream of the ascent region. To disentangle individual uncertainty contributions, we build a high-resolution 70-member perturbed parameter ensemble (PPE) with the Icosahedral Nonhydrostatic (ICON) modelling framework. The PPE systematically combines parameter perturbations and samples the phase space spanned by parameter uncertainty ranges. Based on the PPE, computationally cheap statistical surrogate models are developed that subsequently facilitate variance-based sensitivity analysis for the target variables. Our results suggest that changes to environmental conditions controlling WCB inflow properties most strongly influence WCB ascent behaviour, total surface precipitation sums, and the ridge amplitude. Yet, the microphysical perturbations locally modify vertical velocity along WCB ascent and determine the precipitation efficiency, which affects meso-scale precipitation characteristics as well as the spatial distribution and intensity of precipitation. Moreover, the microphysical perturbations distinctly influence the large-scale flow pattern, albeit to a lesser extent than the perturbations applied to the WCB inflow characteristics.

KEYWORDS

cloud microphysics, Gaussian process emulation, ICON model, large-scale, latent heat, numerical weather prediction, perturbed parameter ensemble, sensitivity experiments, warm conveyor belt

1 | INTRODUCTION

Warm conveyor belts (WCBs) are strongly ascending, cloud-producing, and precipitating airstreams in extratropical cyclones (e.g., Eckhardt *et al.*, 2004; Madonna *et al.*, 2014; Wernli & Davies, 1997). They play an important role for numerical weather prediction (NWP; Rodwell *et al.*, 2017) as they produce a large part of the surface precipitation in extratropical cyclones (Pfahl *et al.*, 2014) and as their interaction with the large-scale upper level flow can influence the downstream ridge characteristics and Rossby wave evolution (e.g., Grams & Archambault, 2016; Joos & Forbes, 2016; Mazoyer *et al.*, 2021; Oertel *et al.*, 2023b; Pomroy & Thorpe, 2000; Rivière *et al.*, 2021). Thus, the misrepresentation of WCB ascent in NWP models can influence large-scale upper level flow properties and amplify forecast errors (Schäfler & Harnisch, 2015; Grams *et al.*, 2018; Berman & Torn, 2019; Oertel *et al.*, 2020; Berman and Torn, 2022; Pickl *et al.*, 2023). The WCB impact on the downstream ridge amplification can be linked to errors in direct potential vorticity modification (Joos & Forbes, 2016; Mazoyer *et al.*, 2021; Pomroy & Thorpe, 2000) and/or in the upper level divergent outflow (Baumgart *et al.*, 2019; Grams & Archambault, 2016; Martínez-Alvarado *et al.*, 2014; Steinfeld & Pfahl, 2019; Teubler & Riemer, 2021), which is associated with latent heating during cloud formation (e.g., Baumgart *et al.*, 2019; Riemer & Jones, 2010). The total latent heating during WCB ascent is substantially determined by cloud microphysical processes (Joos & Wernli, 2012; Martínez-Alvarado *et al.*, 2014; Oertel *et al.*, 2023a).

To date, the representation of cloud microphysics in NWP models is associated with large uncertainties (Dearden *et al.*, 2016; Hande & Hoose, 2017; Khain *et al.*, 2015). Sensitivity studies have shown that changing the cloud microphysics scheme can influence WCB ascent, which also propagates perturbations to the large-scale upper level flow (Joos & Forbes, 2016; Mazoyer *et al.*, 2021, 2023). Further case study evidence suggests that WCB ascent and diabatic heating are sensitive to environmental conditions (Boutle *et al.*, 2011; Schäfler & Harnisch, 2015; Berman & Torn, 2019, 2022), model physics perturbations (Pickl *et al.*, 2022, 2023), model resolution (Choudhary & Voigt, 2022), and in particular to the detailed representation of cloud microphysical processes (Forbes & Clark, 2003; Hieronymus *et al.*, 2022; Joos & Forbes, 2016; Mazoyer *et al.*, 2021, 2023; Neuhauser *et al.*, 2023). As the WCB ascends from near-surface into the upper troposphere, liquid-, mixed-, and ice-phase microphysics interact (e.g., Gehring *et al.*, 2020; Joos & Wernli, 2012; Mazoyer *et al.*, 2021; Oertel *et al.*, 2023a), and sensitivities of WCB ascent to the parametrisations of mixed- (Mazoyer *et al.*, 2023) and ice-phase (Mazoyer *et al.*, 2021) processes have been documented.

Both total and extreme precipitation in the midlatitudes are modulated by WCB occurrence (Pfahl *et al.*, 2014). Although the WCB is often depicted as a stratiform cloud-producing airstream, embedded convection can locally increase precipitation rates (Crespo & Posselt, 2016; Oertel *et al.*, 2019, 2020, 2021). Precipitation formation along WCB ascent can be slightly delayed in polluted conditions with high aerosol concentrations (Joos *et al.*, 2017). Yet, the impact of aerosols on precipitation rates in a coarse-resolution model simulation was found to be rather small (Joos *et al.*, 2017). Besides, the rain rate in extratropical cyclones is generally constrained by moisture influxes into the cyclone (Dacre *et al.*, 2019), and the cloud liquid water path also adjusts to changes in the cloud droplet number concentration (McCoy *et al.*, 2018).

In NWP, uncertainty can be introduced by initial condition (IC) uncertainty and parametric uncertainty arising from an imperfect observation-assimilation system and the need for parametrisation of subgrid-scale physics processes. The individual impact of specific parametrised processes on uncertainties in NWP can be quantified with classical sensitivity experiments—for example, see Joos and Forbes (2016); Joos et al. (017); Mazoyer *et al.* (2021); Rivière *et al.* (2021); Choudhary and Voigt (2022); Wimmer *et al.* (2022); Mazoyer *et al.* (2023) for WCB case studies—which typically cannot sample the full phase space spanned by the uncertainty ranges of model parameters. The recent emergence of perturbed parameter ensembles (PPEs; see Section 2.2.1) for cloud microphysical applications (e.g., Glassmeier *et al.*, 2019; Hoffmann *et al.*, 2020; Johnson *et al.*, 2015; Lee *et al.*, 2011; Wellmann *et al.*, 2018, 2020) facilitates a relatively dense sampling of a multiparameter phase space with a comparatively small number of computationally expensive NWP simulations.

To our knowledge, this study for the first time applies a PPE approach to a WCB case study combining perturbations to poorly constrained cloud microphysical model parameters, aerosol concentrations, and thermodynamic properties in the lower troposphere. The PPE approach combined with subsequent variance-based sensitivity analysis allows the disentanglement of different sources of uncertainty and quantification of the perturbations' impacts for (a) WCB ascent, (b) associated surface precipitation structures, and (c) characteristics of the amplified downstream ridge. Thereby, we illustrate how small-scale perturbations can project to a larger scale and thereby contribute to enhanced process understanding of error growth with implications for constraints on and further development of model physics parametrisations, as well as of ensemble configurations.

Specifically, we address the following questions:

1. How does uncertainty in cloud microphysical parameters and environmental conditions relevant for cloud formation influence the representation of WCB ascent and which parameter perturbations dominate the changes in WCB ascent characteristics?
2. How do the parameter perturbations influence properties of the cloud system, specifically the precipitation structure?
3. Do the perturbations affect the evolution of the larger scale flow and, consequently, demonstrate potential for downstream impact?

The article is structured as follows. We first briefly introduce the numerical model (Section 2.1) and the analysis framework, including the PPE, Gaussian process emulation, and variance-based sensitivity analysis (Section 2.2). Before presenting the sensitivity of WCB ascent to cloud microphysical parameters and environmental conditions (Section 4), the evolution of PPE spread is characterised (Section 3). Subsequently, we show how the parameters influence forecast properties, specifically precipitation characteristics (Section 5) and the simulation of the large-scale flow pattern (Section 6), before concluding with a summary (Section 7).

2 | METHODS

To quantify the uncertainty related to microphysical processes, we perform systematic sensitivity experiments with the Icosahedral Nonhydrostatic (ICON) modelling framework (Zängl *et al.*, 2015) for a WCB case study occurring in October 2016 during the North Atlantic Waveguide and Downstream Impact Experiment (NAWDEX) campaign (IOP 7; Schäfler *et al.*, 2018). The sensitivity experiments include perturbations to five selected parameters, which represent uncertain microphysical model parameters and environmental conditions relevant for cloud formation. In the following, we first describe the NWP model set-up before outlining the analysis framework.

2.1 | NWP model ICON

The ICON model set-up and applied online diagnostics closely follow the approach by Oertel *et al.* (2023a). A global ICON simulation (version 2.6.2.2; Zängl *et al.*, 2015) with approximately 13 km effective grid spacing (R03B07 grid) is run freely for 72 hr with a time step of 120 s. The simulation is initialised from the European Centre for Medium-Range Weather Forecasts (ECMWF) analysis at 1800 UTC on October 3, 2016. Two higher resolution nests with approximately 6.5 km (R03B08 grid) and 3.3 km (R03B09 grid) effective grid spacing, with time steps of 60 s and 30 s respectively, are coupled to the global simulation via two-way feedback (Oertel *et al.*, 2023a; Zängl *et al.*, 2022). The higher resolution nests encompass the WCB ascent region (Figure 1) and facilitate a more detailed representation of microphysical processes, which are parametrised by a two-moment microphysics scheme (Seifert & Beheng, 2006a) with six prognostic hydrometeor types (cloud liquid, q_c; ice, q_i; rain, q_r; snow, q_s; graupel, q_g; and hail, q_h), and their corresponding number concentrations. For an overview of individual microphysical process rates, we refer to Oertel *et al.* (2023a, section 2.2). Further, the ICON default parametrisation schemes are used for turbulence (Raschendorfer, 2018), subgrid-scale orographic drag (Lott & Miller, 1997), and non-orographic gravity wave drag (Orr *et al.*, 2010). Radiative transfer is parametrised by the ecRad scheme (Hogan & Bozzo, 2018). Shallow convection is parametrised in all domains, and deep convection is treated explicitly in the refined nests and parametrised with the Tiedtke–Bechtold convection scheme (Bechtold *et al.*, 2008; ECMWF, 2016; Tiedtke, 1989) in the global domain.

We use a Lagrangian framework to identify WCB trajectories through an ascent criterion of at least 600 hPa in 48 hr (Madonna *et al.*, 2014; Wernli & Davies, 1997). To capture smaller scale heterogeneities and rapid, convective ascent embedded in the WCB (Blanchard *et al.*, 2020; Oertel *et al.*, 2020, 2021; Rasp *et al.*, 2016), as well as perturbations from microphysical processes (Mazoyer *et al.*, 2021; Miltenberger *et al.*, 2016, 2020), we employ high-resolution online trajectories (Oertel *et al.*, 2023a), which are calculated during the simulation using wind fields on the original model grid at each time step. Trajectory positions are calculated from the resolved wind fields in the nest with the highest spatial resolution at a given geolocation and using the corresponding model time step; see Oertel *et al.* (2023a) for details. Moreover, the trajectories are able to enter and leave the refined nests.

Following Oertel *et al.* (2023a), online trajectories are started every 1 hr during the 72 hr simulation from six vertical levels between 200 and 1,500 m, and approximately 1,900 longitude and latitude positions between −55°E to −15°E and 35°N–55°N predefined based on offline WCB calculations with LAGRANTO (Sprenger & Wernli, 2015). In total, approximately 820,000 trajectories are started in every simulation from the same positions. Trajectory positions and properties, such as pressure, temperature, and diabatic heating rates, are output every 1 hr (see Supporting Information Table A1 for list of available variables along online trajectories). From all the trajectories, we only

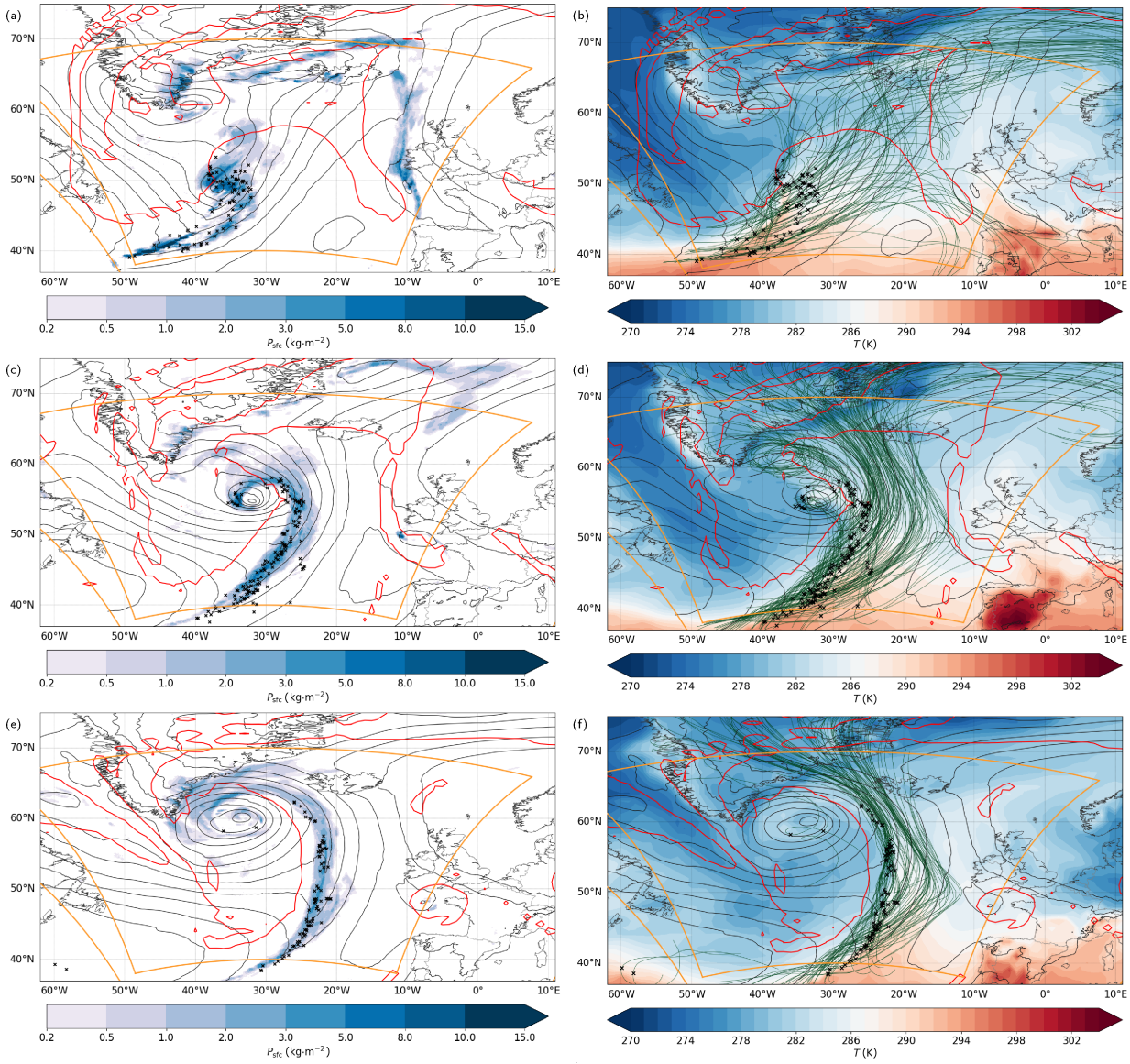

FIGURE 1 Synoptic evolution of the warm conveyor belt (WCB) case on (a, b) October 4 at 0600 UTC, (c, d) October 4 at 1800 UTC, and (e, f) October 5 at 0600 UTC. (a, c, e) The 1-hr surface precipitation P_{sfc} (kg · m^{-2}) and mean-sea-level pressure (grey contours, every 5 hPa) from the second domain, as well as the dynamical tropopause (2 PVU at 320 K; red contour) taken from the global domain. Black markers denote WCB air parcel positions from WCB trajectories that started their ascent 6 hr prior to the times shown (only every 10th WCB trajectory is shown). The orange lines indicate the extent of both refined nests. (b, d, f) Temperature T (K) at 1,000 hPa taken from the global domain and WCB trajectories that started their ascent 6 hr prior to the time shown (green; only every 10th WCB trajectory is shown). WCB air parcel positions are indicated as in (a), (c), and (e). Also shown are mean-sea-level pressure (grey contours, every 5 hPa) and the dynamical tropopause (red). All fields are taken from the unperturbed reference simulation.

select those that fulfil the ascent criterion of 600 hPa in 48 hr as WCB trajectories. The WCB ascent phase is subsequently defined as the period with the fastest 600 hPa ascent and described in the following by the associated characteristic ascent time-scale (τ_{600}; Oertel *et al.*, 2021, 2023a).

Figure 1 shows the synoptic evolution of the WCB case, which is described in more detail in Oertel *et al.* (2023a). The surface cyclone, which is associated with the WCB cloud band, originates from the western North Atlantic and has propagated across the North Atlantic before developing clear frontal structures. The WCB airstream is associated with an extended cloud band and surface precipitation in the cyclone's warm sector (Figure 1a,c,e). On October 4 and 5, WCB trajectories ascend primarily ahead of the cold front and the upper level trough located in the central North Atlantic south of Greenland (Figure 1b,d,e). The WCB trajectories ascend into the downstream ridge, which amplifies over the eastern North Atlantic and Europe (Figure 1d,f).

2.2 | Sensitivity experiments

We quantify sensitivities to five uncertain input parameters (i.e., the number of perturbed input parameters $N_P = 5$). To systematically cover the full parameter space from five selected uncertain parameters, a large number of simulations is required where each simulation combines different input parameter values. Such simulations ideally cover the entire phase space spanned by the uncertain parameters with a fairly dense sampling. As such an approach is not feasible with a computationally expensive NWP model, we employ statistical emulation, which is based on building fast and computationally cheap statistical surrogate models, the emulator, that can be used to explore the entire phase space spanned by the uncertain input parameters. The surrogate models are trained on a PPE, in which numerically expensive full NWP ensemble members optimally explore the entire phase space spanned by the uncertain input parameters. Subsequently, surrogate models can be built independently for selected model output variables ("target variables"), such that the target variable (see Table 3) can be approximated from the emulator using very densely spaced input parameter combinations.

The following briefly outlines the applied method that follows Lee *et al.* (2011); Johnson *et al.* (2015); Wellmann *et al.* (2018, 2020).

1. A (relatively) large number of simulations with the numerically expensive NWP model ICON using optimal parameter combinations for $N_P = 5$ uncertain parameters is conducted (Section 2.2.1). These form the PPE.
2. Computationally cheap statistical surrogate models are developed for carefully selected target variables using multidimensional Gaussian process emulation (Section 2.3).
3. The statistical surrogate models are used for variance-based sensitivity analysis, which quantifies the individual contributions of each uncertain parameter for the total uncertainty in the target variable (Section 2.4). Variance-based sensitivity analysis requires a very large number of simulations, which can only be realised with a computationally cheap statistical surrogate model.

2.2.1 | Perturbed parameters

The PPE comprises 70 individual members (Section 2.2.2) whereby each member includes combined perturbations to $N_P = 5$ uncertain model parameters $\mathbf{X} = \{X1, X2, \ldots, X5\}$. "Parameter" here refers to a scalar model quantity that can be independently perturbed and influences WCB ascent and associated cloud formation. The parameters selected represent uncertain parameters prescribed in the applied two-moment microphysics scheme, as well as particularly uncertain environmental conditions relevant for cloud microphysical processes and WCB ascent. Specifically, we perturb cloud condensation nuclei (CCN) and ice nucleating particle (INP) concentrations, which are prescribed in ICON and most NWP systems, and thus represent parametric uncertainty. We further perturb the capacitance (CAP) parameter, which influences vapour deposition onto ice and snow, and the maximum possible supersaturation (SAT) with respect to liquid. Uncertainty in thermodynamic boundary conditions is introduced through changes to sea-surface temperature (SST), which modifies WCB inflow specific humidity and temperature. Parameter selection is based on prior knowledge of relevant processes for diabatic heating in the WCB (Oertel *et al.*, 2023a) and also takes into account which model parameters are particularly poorly constrained. Parameters and their ranges are defined based on literature, a previous detailed analysis of the case study, and expert solicitation, and are described subsequently herein and in Table 1. In addition to the 70 PPE members, we include one unperturbed reference and eight so-called end-member simulations with one-at-a-time parameter perturbations and the respective maximum parameter ranges (Table 2).

CCN

The representation of cloud droplet activation (i.e., the activation of aerosol particles to cloud droplets) influences the subsequent microphysical process rates and dynamical response of cloud systems (e.g., Barrett & Hoose, 2023; Barthlott *et al.*, 2022; Barthlott & Hoose, 2018; Noppel *et al.*, 2010; Seifert & Beheng, 2006b; Wellmann *et al.*, 2018).

The cloud droplet activation scheme applied (Hande et al., 2016) assumes a vertical CCN profile that decays with height, and droplet activation explicitly scales with the grid-scale vertical velocity. The assumed vertical CCN profile is invariant in time, although CCN concentrations can vary substantially depending on local air-mass origin (Hudson & Xie, 1999; Watson-Parris *et al.*, 2019), season (Hande et al., 2016; Wang *et al.*, 2021), or synoptic conditions (Wang *et al.*, 2021). The parametrisation for cloud droplet activation applied has been modified from ICON's default two-moment scheme—originally developed for continental Germany by Hande et al. (2016)—to account for CCN concentrations over the Atlantic; see Oertel

TABLE 1 Overview of uncertain parameters and their ranges for the perturbed parameter ensemble. The perturbed parameters represent variations in sea-surface temperature (SST), cloud condensation nuclei concentration (CCN), ice nucleating particle concentration (INP), capacitance of snow and ice (CAP), and maximum supersaturation with respect to liquid (SAT). The processes directly influenced by the parameters are also named.

Parameter	Min	Max	Unit	Process
SST	−2	+2	K	Latent and sensible heat fluxes over sea surface
CCN	0.4	20	Scaling factor	Cloud droplet activation
INP	0.01	20	Scaling factor	Ice nucleation (immersion and deposition, freezing of rain)
CAP	0.2	1	Scaling factor	Growth of ice/snow by vapour deposition
SAT	0	0.1	—	Condensation from saturation adjustment scheme

TABLE 2 Overview of end-member simulations and their respective parameter perturbations. The parameters f_{CCN}, f_{INP}, and f_{CAP} are multiplicative (i.e., 1 corresponds to the unperturbed state), whereas f_{SST} and f_{SAT} are additive (i.e., 0 corresponds to the unperturbed state)

End member	f_{SST}	f_{CCN}	f_{INP}	f_{CAP}	f_{SAT}
REF	0	1	1	1	0
SST+	2	1	1	1	0
SST−	−2	1	1	1	0
CCN+	0	20	1	1	0
CCN−	0	0.4	1	1	0
INP+	0	1	20	1	0
INP−	0	1	0.01	1	0
CAP−	0	1	1	0.2	0
SAT+	0	1	1	1	0.1

Note: SST: sea-surface temperature; CCN: cloud condensation nuclei concentration; INP: ice nucleating particle concentration; CAP: capacitance of snow and ice; SAT: supersaturation with respect to liquid.

et al. (2023a) for details. The number of activated cloud droplets N_c depends on vertical velocity w ($m \cdot s^{-1}$) and pressure p (hPa), and is defined following Equation (1), with prescribed pressure-dependent coefficients $N_a(p)$, $B(p)$, and $C(p)$:

$$N_c(w,p) = N_a(p)[1 + e^{-B(p)\times\ln(w)-C(p)}]^{-1}, \quad (1)$$

with

$$N_a(p) = \begin{cases} (250+7)\ \mathrm{cm}^{-3} & \text{if } p \geq 800\ \mathrm{hPa}, \\ [250 \times e^{(p-800\ \mathrm{hPa})/150\ \mathrm{hPa}} & \\ +7 \times e^{(p-800\ \mathrm{hPa})/400\ \mathrm{hPa}}]\ \mathrm{cm}^{-3} & \text{else}, \end{cases}$$

and

$$B(p) = b_1 \times e^{-b_2\times p+b_3}$$
$$C(p) = c_1 \times e^{-c_2\times p+c_3}$$

$$b_1 = 3.46281429 \times 10^0,\ b_2 = 1.74926665 \times 10^{-4},$$
$$b_3 = -2.85967514 \times 10^{-10}$$
$$c_1 = 2.72664755 \times 10^0,\ c_2 = 1.12852352 \times 10^{-3},$$
$$c_3 = 1.50069026 \times 10^0.$$

To account for the uncertainty in the representation of CCN concentrations, the number of activated cloud droplets per time step $N_c(w,p)$ is scaled by a factor f_{CCN} that varies between 0.4 and 20 and approximately represents observed CCN variability ranges (e.g., Wylie & Hudson, 2002; Hande *et al.*, 2015, 2016; Genz *et al.*, 2020; Wang *et al.*, 2021). This results in CCN concentrations ranging between approximately $N_c = 100\ \mathrm{cm}^{-3}$ and $5,000\ \mathrm{cm}^{-3}$ respectively in the limit of large vertical velocities and in the lower troposphere (i.e., for pressure values larger than 800 hPa). In the unperturbed reference, N_c amounts to approximately $250\ \mathrm{cm}^{-3}$; see Oertel *et al.* (2023a, Fig. 2).

INP

INP concentrations primarily influence the number of newly formed ice particles through heterogeneous freezing and are prescribed by temperature-dependent functions following Hande *et al.* (2015), although, similar to CCN concentrations, their concentrations in the atmosphere can vary across several magnitudes (DeMott *et al.*, 2010; Hande *et al.*, 2015). To account for uncertainty in their representation, three processes that are influenced by INP concentrations are scaled with a factor f_{INP}: immersion freezing of cloud droplets (Hande *et al.*, 2015), deposition nucleation of cloud ice (Hande *et al.*, 2015), and freezing of raindrops (Bigg, 1953). In each PPE member, the same scaling factor is applied to all three processes, and all freezing rates are varied on a logarithmic scale within the range of 0.01 to 20. Thus, for example, at −15°C and 110% relative humidity over ice, the immersion freezing INP concentration varies between $< 1\ \mathrm{m}^{-3}$ and $\sim 100\ \mathrm{m}^{-3}$ ($5\ \mathrm{m}^{-3}$ for the unperturbed reference).

CAP

The capacitance (CAP) of frozen hydrometeors determines the efficiency of water vapour deposition onto their surface and captures both the solid particle's habit and its size (Westbrook & Heymsfield, 2011). Hence, the value of CAP chosen influences the rate of depositional growth of ice and snow, and thus ice and snow water content (e.g., Lin & Colle, 2011), as well as associated latent heating. Theory predicts that, for spheres, CAP is largest and equals the radius (CAP = $0.5D$, with D the diameter). However, the habit of ice crystals is very heterogeneous, and the normalised CAP (CAP/D) depends on the aspect ratio (e.g., Chiruta & Wang, 2005; Westbrook *et al.*, 2008; Westbrook & Heymsfield, 2011), such that rosettes, aggregates, or columns often have a reduced CAP (Chiruta & Wang, 2003, 2005). Observations (and in particular the model representation) of normalised CAP values are uncertain, and values range between 0.1 and 0.5 (Lin & Colle, 2011; Westbrook & Heymsfield, 2011). Here, we simultaneously scale CAP of ice and snow with a factor f_{CAP} that varies between 0.2 and 1, which results in normalised CAP values between 0.1 and 0.5. The normalised CAP value for the unperturbed reference amounts to 0.5. Each PPE member includes the same scaling factor for both ice and snow. As graupel and hail approach the shape of a sphere, their CAP is kept constant.

SAT

ICON uses a saturation adjustment scheme (once before and once after the explicit microphysical processes), which establishes thermodynamic equilibrium between water vapour and cloud droplets by condensation or evaporation of cloud droplets respectively. The instantaneous removal of super- or subsaturation assumes that clouds relax instantly to a thermodynamic equilibrium; that is, no supersaturation with respect to liquid is possible (i.e., $q_{\mathrm{v}}/q_{\mathrm{v,s}} \leq 1$, with q_{v} the specific humidity and $q_{\mathrm{v,s}}$ the saturation specific humidity over water). The use of a saturation adjustment on coarser grid scales and with model time steps longer than the characteristic time-scale for condensation is considered adequate (Chuang *et al.*, 1997). However, at higher spatial resolutions, where large vertical velocities may be present, supersaturated conditions can establish. In such cases, the use of a saturation adjustment can artificially increase condensation at lower levels (Lebo *et al.*, 2012) and modify diabatic heating profiles (Igel & Van Den Heever, 2021). As the diabatic heating from the saturation adjustment is a primary heating contribution for WCB ascent and essentially determines diabatic heating during its ascent (Oertel *et al.*, 2023a), we also introduce perturbations to the saturation adjustment by increasing the maximum possible saturation ratio to values > 1. The details of CCN activation and cloud base supersaturation cannot be resolved at the vertical grid spacings and time steps used in our set-up. However, after CCN activation, supersaturation can be shown to approach an equilibrium value, which is determined by updraught velocity and diffusional growth of cloud particles (for a time-invariant updraught velocity). Based on this consideration, we introduce a dynamic supersaturation scaling, Equation (2), which allows supersaturation depending on local vertical velocity. Thereby, higher supersaturation can be established in faster updraughts (Korolev & Mazin, 2003; Morrison & Grabowski, 2008).

To dynamically increase the saturation ratio S ($S = q^*_{\mathrm{v,s}}(T,p)/q_{\mathrm{v,s}}(T,p)$), the critical specific humidity threshold to equilibrate water vapour and cloud droplets $q^*_{\mathrm{v,s}}(T,p)$ is set to

$$q^*_{\mathrm{v,s}}(T,p) = [1 + (f_{\mathrm{SAT}} w)] q_{\mathrm{v,s}}(T,p) | w > 0. \quad (2)$$

The scaling factor f_{SAT} that is applied to the critical saturation specific humidity $q^*_{\mathrm{v,s}}(T,p)$ varies in the range of 0 to 0.1. The default is $f_{\mathrm{SAT}} = 0$, which simply uses the saturation specific humidity $q_{\mathrm{v,s}}(T,p)$ at temperature T and pressure p as critical threshold for q_{v}, that is the standard

saturation adjustment approach. Equilibrium supersaturation is approximately on the order of $f_{SAT} \sim 0.001$, given the median estimated cloud droplet radius and low number concentrations estimated from this case study. To analyse the effect of very extreme supersaturation values in pristine conditions, maximum f_{SAT} values for the sensitivity experiments are set to 0.1.

SST

The lower tropospheric humidity in the WCB inflow region is important for its subsequent ascent (Schäfler & Harnisch, 2015; Quinting & Grams, 2021, 2022; Berman & Torn, 2019, 2022; Dacre *et al.*, 2019; Boettcher *et al.*, 2021) and can, for example, be modulated by the representation of the underlying SST (Christ *et al.*, 2025). Errors in the model representation of inflow specific humidity can influence total diabatic heating in the WCB and subsequently also the upper level flow (Schäfler & Harnisch, 2015; Berman and Torn, 2022; Christ *et al.*, 2025). Specific humidity errors in the WCB inflow region in NWP models can amount to up to 1–2 $g \cdot kg^{-1}$ (Schäfler *et al.*, 2011; Schäfler & Harnisch, 2015). Moreover, the low-level stability (e.g., vertical θ_e gradient) is important for detailed WCB ascent behaviour and in particular can modify the fraction of rapidly ascending WCB trajectories (Oertel *et al.*, 2019, 2021). To analyse the sensitivity to the temperature and moisture availability in the WCB inflow, we modify SST using a constant offset in the range of ±2 K, which continuously changes surface latent and sensible heat fluxes throughout the simulation, and hence gradually influences low-level specific humidity and temperature, and thus θ_e (see also Sánchez *et al.*, 2024). As free-running simulations are used, SST, instead of ICs, were modified to avoid that the additional moisture and temperature perturbations are immediately removed during model spin-up through the introduced imbalances. In NWP simulations with the ICON model, SST is by default kept constant during the simulation. The reference SST is taken from the analysis of ECMWF's Integrated Forecasting System (IFS) at initial time and subsequently perturbed globally.

At 50°N, an SST difference of 4 K corresponds approximately to a 5–10° poleward shift (Roberts *et al.*, 2021), and could also be interpreted as uncertainty in cyclone position and WCB inflow location. In subseasonal forecasts, substantial local SST biases of ±2 K can emerge and are particularly large in the Gulf Stream region, which impacts forecasts of the North Atlantic circulation and Northern Hemispheric waveguide (Roberts *et al.*, 2021). Understanding the local SST impacts on WCB ascent and downstream flow evolution can also mechanistically link SST and boundary-layer processes to the midlatitude upper level circulation (e.g., Czaja, 2019; Kwon *et al.*, 2020; Roberts *et al.*, 2020, 2021, 2022; Schemm, 2023; Wenta *et al.*, 2024).

2.2.2 | Design of experiments

To optimally cover the five-dimensional phase space spanned by the uncertain parameters, optimal parameter perturbations within the predefined parameter ranges (Section 2.2.1) for the sensitivities are determined using Latin hypercube sampling (Morris & Mitchell, 1995; Stein, 1987), which maximises the minimum distance between the input parameter combinations (Feingold *et al.*, 2016) and results in a uniform distribution of parameter values. We use $N = 10 \times N_P$ input parameter combinations (where N_P is the number of perturbed input parameters) to train the emulator; that is, 50 initial parameter value combinations are used for simulations with the full NWP model set-up (Johnson *et al.*, 2015; Loeppky *et al.*, 2009). The simulations for the validation dataset are obtained by extending the initial 50 input parameter combinations by 20 additional simulations ($N = 4 \times N_P$), which optimally fill the gaps in the phase space occupied by the existing 50 parameter combinations. After the augmentation, the resulting 70 parameter perturbations also represent a Latin hypercube. The R package "LHS" (Carnell, 2024) was used for the Latin hypercube design.

2.3 | Gaussian process emulation

Gaussian process emulation (O'Hagan, 2006; Rasmussen, 2004; Rasmussen & Williams, 2006) is used to develop statistical surrogate models for selected target variables Y, such that Y can be approximated with the emulator for any given input parameter value combination $\mathbf{x} = \{x1, x2, \ldots, x5\}$ within the specified parameter ranges. In atmospheric sciences, Gaussian process emulation has been successfully applied to understand parametric uncertainty and uncertainty related to boundary/background conditions in numerical models (e.g., Glassmeier *et al.*, 2019; Hoffmann *et al.*, 2020; Johnson *et al.*, 2015; Lee *et al.*, 2011; Posselt *et al.*, 2016; Wellmann *et al.*, 2018, 2020).

A Gaussian process is a generalisation of the multivariate Gaussian distribution to an infinite number of variables (Rasmussen, 2004). The Bayesian method can be used to estimate multidimensional relationships from sparse, but smoothly varying data. It is described by a mean function $m(\mathbf{x})$, where $\mathbf{x} = \{x1, x2, \ldots, x5\}$ represent the uncertain input parameter values, and a covariance structure $V(\mathbf{x},\mathbf{x}')$:

TABLE 3 Overview of target variables diagnosed from the perturbed parameter ensemble members classified in target variables characterising warm conveyor belt (WCB) ascent (Section 4), precipitation (Section 5), and large-scale flow patterns (Section 6). See text for details.

Variable symbol	Variable description	Lagrange/Eulerian
N_{tra}	Number of WCB trajectories	Lagrange
τ_{600}	Mean ascent time-scale	Lagrange
f_{3h}	Fraction of trajectories with ascent time-scale below 3 hr	Lagrange
f_{10h}	Fraction of trajectories with ascent time-scale below 10 hr	Lagrange
ADH	Total WCB ascent integrated diabatic heating	Lagrange
w_{cp}/w_{wp}	Local maximum of cold-phase/warm-phase ascent velocity along WCB ascent	Lagrange
θ_{cp}/θ_{wp}	Local maximum of cold-phase/warm-phase diabatic heating rate along WCB ascent	Lagrange
P_{24h}, P_{36h}, P_{48h}, P_{72h}	24-hr, 36-hr, 48-hr, 72-hr integrated surface precipitation sum	Eulerian
MPE	Microphysical precipitation efficiency	Eulerian
LPE	Lagrangian precipitation efficiency estimate	Lagrange
$P_{99.9}$	Precipitation intensity	Eulerian
PC1 (Z300),* PC1 (Z500)*	Principal component for EOF 1 for geopotential at 300 and 500 hPa at lead times 24, 48, and 72 hr	Eulerian
PC2 (Z300),* PC2 (Z500)*	Principal component for EOF 2 for geopotential at 300 and 500 hPa at lead times 24, 48, and 72 hr	Eulerian
PC3 (Z300),* PC3 (Z500)*	Principal component for EOF 3 for geopotential at 300 and 500 hPa at lead times 24, 48, and 72 hr	Eulerian

Note: Target variables denoted with an asterisk are analysed but no variance decomposition is explicitly performed. EOF: empirical orthogonal function.

$$Y \sim \mathrm{GP}[\mathbf{m}(\mathbf{x}), V(\mathbf{x},\mathbf{x}')],$$
$$m(\mathbf{x}) = \mathbf{h}(\mathbf{x})^{\mathrm{T}}\boldsymbol{\beta},$$
$$V(\mathbf{x},\mathbf{x}') = \sigma^2 c(\mathbf{x},\mathbf{x}'),$$

where $\mathbf{h}(\mathbf{x})$ contains known regression functions of $\mathbf{x}$, and $\boldsymbol{\beta}$ consists of unknown coefficients that are fitted during the training of the emulator. We use a linear mean function. The covariance structure, which defines the covariance in the target variable Y for any pair of input parameter combinations $\mathbf{x}$ and $\mathbf{x}'$, is specified by a scale parameter σ^2 and a correlation function, $c(\mathbf{x},\mathbf{x}')$, which is here chosen to be the Matérn correlation as it can cope with slightly rougher surfaces than the squared exponential correlation (Johnson *et al.*, 2015; Rasmussen & Williams, 2006). The unknown hyperparameters of the Gaussian process are estimated from the training data using a maximum likelihood method.

We build independent Gaussian process emulators for several target variables (see Table 3) that are described in detail in Sections 4–6. For the training and validation of the emulator, the entire 70-member PPE was split into a training dataset, comprising the first 50 members, and a validation dataset, comprising the remaining 20 members. The quality of the individual emulators is evaluated by comparing the emulator predictions for the independent validation data with the corresponding direct model output following Johnson *et al.* (2015) and Wellmann *et al.* (2018). The predicted values, and their 95% confidence intervals, lie close to the line of equality, indicating a reasonable model fit (Figure 2). An inherent property of a Gaussian process is that the predicted target variable values for the training dataset are identical to their real values (Figure 2; see also Lee *et al.*, 2011).

The computationally cheap and fast emulator can be used to establish a dense sampling of the variation of the target variable across the entire five-dimensional phase space spanned by the uncertain input parameters and their predefined ranges. The dense random sampling allows for variance analysis and thereby for a quantification of the contribution of each uncertain parameter to the total variance of a target variable across the entire phase space (see Section 2.4). In particular, we use the emulator to generate a total of 50,000 (i.e., 10,000 per perturbed parameter) predictions. To illustrate the methodology, Figure 3 shows the emulator predictions for the target variable "number of WCB trajectories" N_{tra}. Both the ICON data (orange

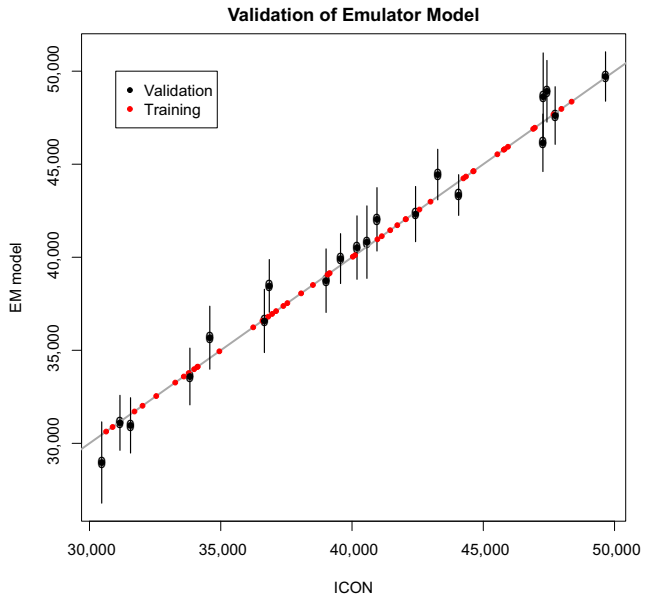

FIGURE 2 Validation of the fitted Gaussian process for the number of trajectories N_{tra}. Emulator predictions for N_{tra} and according 95% confidence intervals versus N_{tra} from the ICON simulations for the validation data (black). The emulator predictions for the training data are shown in red, visualising the perfect fit of a Gaussian process emulator for the training data.

markers) and the emulator simulations (black line and shading show mean and standard deviation of 50,000 emulator predictions) suggest that N_{tra} linearly increases with increasing SST within the perturbed range. Moreover, a smaller influence from CCN and INP is evident, whereas no systematic impact from CAP and SAT perturbations is discernible.

2.4 | Variance-based sensitivity analysis

The variance of a specific target variable across an ensemble is a commonly used measure for uncertainty. In the PPE, the uncertainty is introduced by the variations in the input parameter values of the N_P uncertain parameters. For N_P independent input parameters, the total variance V can be decomposed into different contributions (Oakley & O'Hagan, 2004):

$$V = \sum_{i=1}^{N_P} V_i + \sum_{i<j} V_{i,j} + \cdots + V_{1,\ldots,N_P}, \tag{3}$$

where V_i are the contributions from each of the N_P uncertain parameters (in our case $N_P = 5$), and the other terms are the contributions from input parameter interactions.

We define the so-called "main effect" (ME) from each uncertain input parameter as the fraction of variance explained by the parameter considered:

$$\mathrm{ME}_i = \frac{V_i}{V}. \tag{4}$$

The remaining fraction of the sum of all individual main effects $(1 - \sum_{i=1}^{N_P} \mathrm{ME}_i)$ is the interaction effect, which indicates how much the individually perturbed input parameters interact with each other.

We use the R package "sensitivity" (Iooss *et al.*, 2023) and the extended Fourier amplitude sensitivity test (Saltelli *et al.*, 1999) for variance decomposition, which facilitates a global sensitivity analysis but requires a large sample size. The large sample size of several thousands of realisations of the target variable with densely spaced input parameter values is only feasible with the computationally cheap emulators (see Section 2.3). For the variance decomposition, we generate 10,000 predictions of the target variable per uncertain input parameter N_P using the surrogate model. Figure 3f shows the main effects for N_{tra}: SST perturbations explain 90% of total variance in N_{tra} (ME = 90%) within the predefined ranges, and CCN and INP perturbations almost equally contribute approximately 5% and 4% respectively to the total variance in N_{tra}. This is broadly consistent with the behaviours suggested by the scatterplots in Figure 3a–e.

3 | GROWTH OF ENSEMBLE SPREAD IN BASIC METEOROLOGICAL VARIABLES

A commonly used measure to evaluate uncertainty in an ensemble is the ensemble standard deviation, often termed ensemble spread. In this section we illustrate the evolution of ensemble spread in the PPE and compare its evolution with quasi-operational forecasts with ECMWF's IFS, including physics and IC perturbations (Pickl *et al.*, 2022), to qualitatively validate the effect of the parameter perturbations on the PPE ensemble spread. Note that a quantitative validation of the PPE quality and comparison with the quasi-operational IFS ensemble would require boot-strapping to quantify the ensemble spread, accounting for the difference in the number of ensemble members as well as consideration of the spread–error relation. This is, however, beyond the scope of this study, which focuses on the quantification of individual parameter sensitivities.

Operationally, the ECMWF applies both stochastically perturbed parametrisation tendencies (SPPT), an operationally applied technique to increase ensemble spread by perturbing physics tendencies (Leutbecher *et al.*, 2017), and IC perturbations (Buizza *et al.*, 2008; Leutbecher *et al.*, 2017; Leutbecher & Palmer, 2008). These two established perturbation approaches provide a range of reasonable ensemble spread. Here, we qualitatively compare

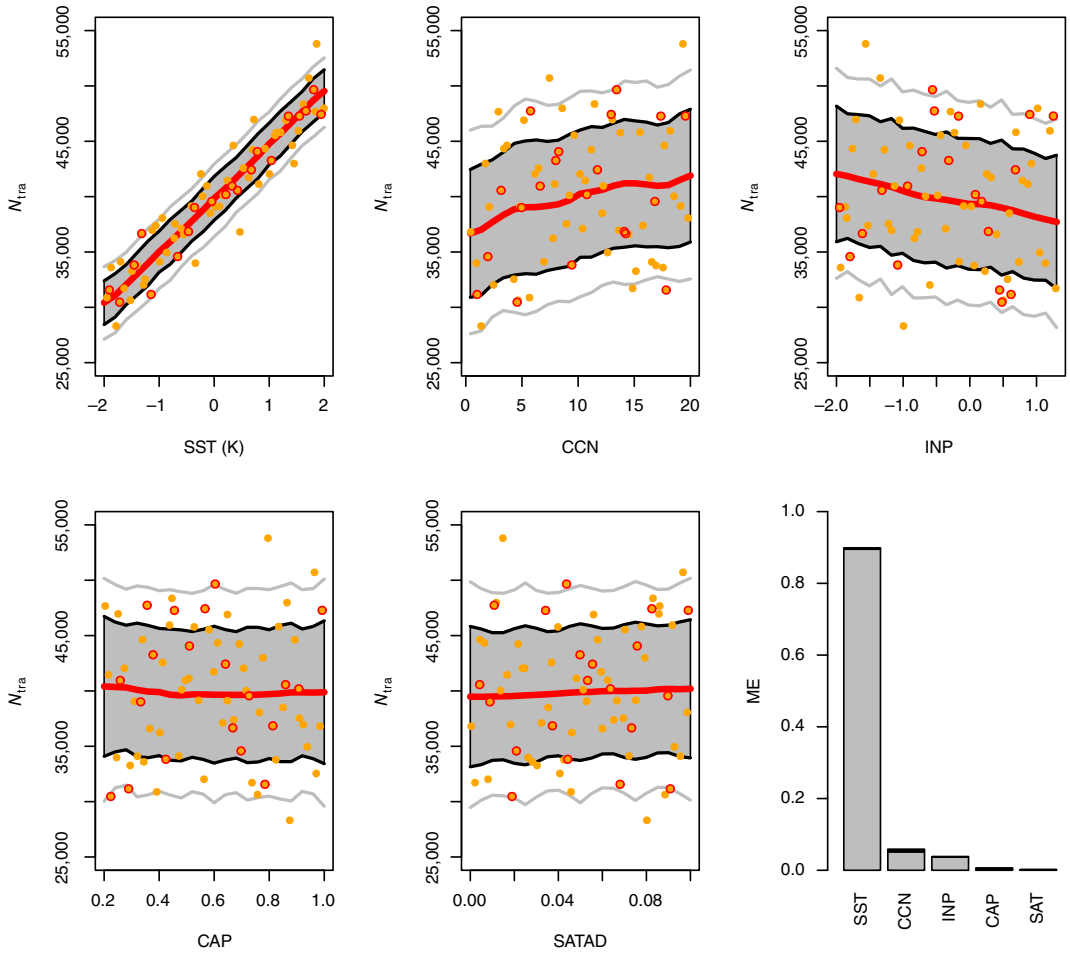

FIGURE 3 Emulator predictions for, in total, $10,000 \times 5$ predictions for the number of warm conveyor belt trajectories N_{tra} with densely spaced input parameters combinations represented as function of (a) sea-surface temperature (SST), (b) cloud condensation nuclei concentration (CCN), (c) ice nucleating particle concentration (INP), (d) capacitance (CAP), and (e) supersaturation (SAT). All predictions include combined perturbations to all parameters within the predefined range. Shown are the mean (red lines), standard deviation (grey shading), and 5th and 95th percentiles (grey lines) from the emulator predictions, as well as the direct ICON output from the training (orange dots) and validation data (orange dots with red border). (f) Fraction of explained variance per input parameter (main effect, ME; grey) including input parameter interaction effects (black).

the PPE with two simulations that include these different perturbation approaches; namely, (a) IC and SPPT ("IFS-IC+SPPT") and (b) SPPT only ("IFS-SPPT only"). The IFS simulations are run with the model version IFS CY46R1 with a TCo399L91 resolution and include 20 perturbed members plus unperturbed control forecast; see (Pickl *et al.*, 2022, for details). The simulations are initialised at 0000 UTC, October 4, 2016; that is, they simulate the same WCB case study. Data are also available on a $1° \times 1°$ grid. The analysis focuses on the spread in 500 hPa geopotential (Z500), which is a metric of the larger scale flow evolution, and on the near-surface temperature and specific humidity, which impact low-level moisture flux into the WCB.

Figure 4 shows the poleward-directed WCB ascent associated with the cyclone south of Greenland (Figure 4a,b) and the downstream ridge amplification over the eastern North Atlantic and Europe (Figure 4c). The parameter perturbations lead to substantial ensemble spread across the PPE that grows with time, as shown by the example for the spread of Z500 interpolated to a regular $1° \times 1°$ (Figure 4). The increase of spread of Z500 is particularly large in the diabatically active regions near and downstream of the WCB ascent region. After 3 days lead time, the ensemble spread is largest at the western edge of the poleward-extended ridge into which the WCB air parcels ascend (Figure 4c). However, despite the combined parameter perturbations, the simulations do not diverge entirely and all PPE members reasonably simulate the WCB ascent and large-scale flow evolution. Overall, the spread of geopotential height averaged across the WCB inflow, ascent, and outflow region remains smaller

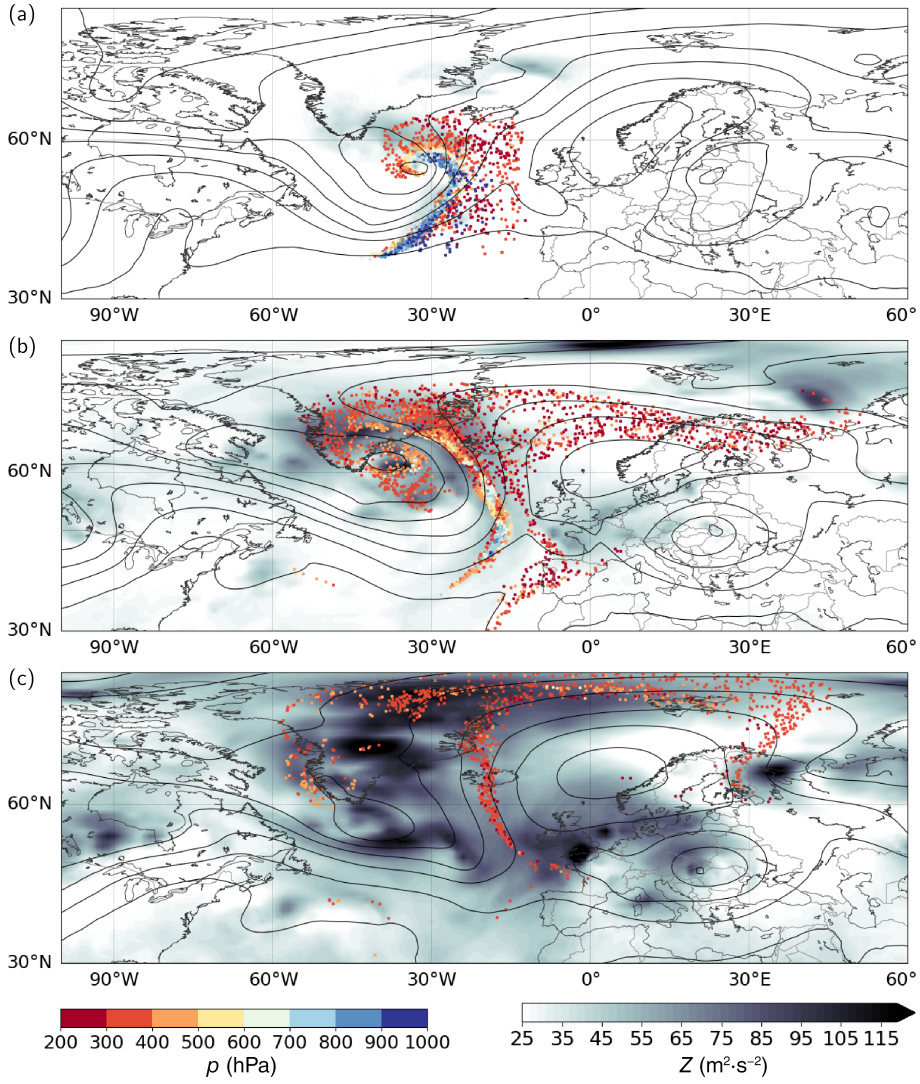

FIGURE 4 Ensemble mean (black) and standard deviation (shading) of 500 hPa geopotential in the 50-member training perturbed parameter ensemble after (a) 24 hr, (b) 48 hr, and (c) 72 hr lead time. Coloured markers show the position and pressure of warm conveyor belt (WCB) air parcels from the unperturbed reference simulation (only every 10th WCB trajectory is shown).

in the PPE than in the quasi-operational "IFS-IC+SPPT" simulations throughout the troposphere and at all lead times (Figure 5a), which can be anticipated because the "IFS-IC+SPPT" ensemble additionally incorporates IC uncertainty. Nevertheless, the emerging spread in the PPE shows that the small-scale microphysical process perturbations as well as the perturbations that are introduced at the surface through SST are projected to the larger scale flow and to higher altitudes (Figure 5a).

The PPE spread is similar to the one from a 21-member IFS ensemble simulation (Figure 5a), which is produced with SPPT. As the IC perturbations in the IFS grow rapidly, the spread in the "IFS-IC+SPPT" is generally larger than in "IFS-SPPT only" and the PPE, and is not equal to zero at initialisation time (in contrast to the spread in "IFS-SPPT only" and the PPE).

The spread of near-surface specific humidity (Figure 5b) grows faster in the PPE than in the "IFS-SPPT only"' (note that SPPT is strongly reduced in the boundary layer and zero at the surface; Leutbecher *et al.* (2017), whereas the growth rate of temperature is slightly smaller in the PPE than in the "IFS-SPPT only" (Figure 5c). Moreover, for the first 2 days' lead time the spread of temperature and specific humidity in the PPE decreases with height, because the latent and sensible heat fluxes, most strongly influenced by SST perturbations, induce growth of spread from the surface (Figure 5b,c). Specifically, warmer SST increases the latent and sensible heat fluxes in the warm and cold sectors of the cyclone, which leads to a moistening and warming of the near surface, such that low-level temperature and specific humidity across the PPE members continuously diverge with increasing lead time.

After several hours lead time, the maximum difference in low-level θ_e (averaged over the WCB ascent region in the North Atlantic at 850 hPa) among all PPE members remains below 1.5 K (not shown).Differences in averaged low-level specific humidity remain below 1 $g \cdot kg^{-1}$ and are well within the range of WCB inflow moisture biases reported by Schäfler and Harnisch (2015). All PPE

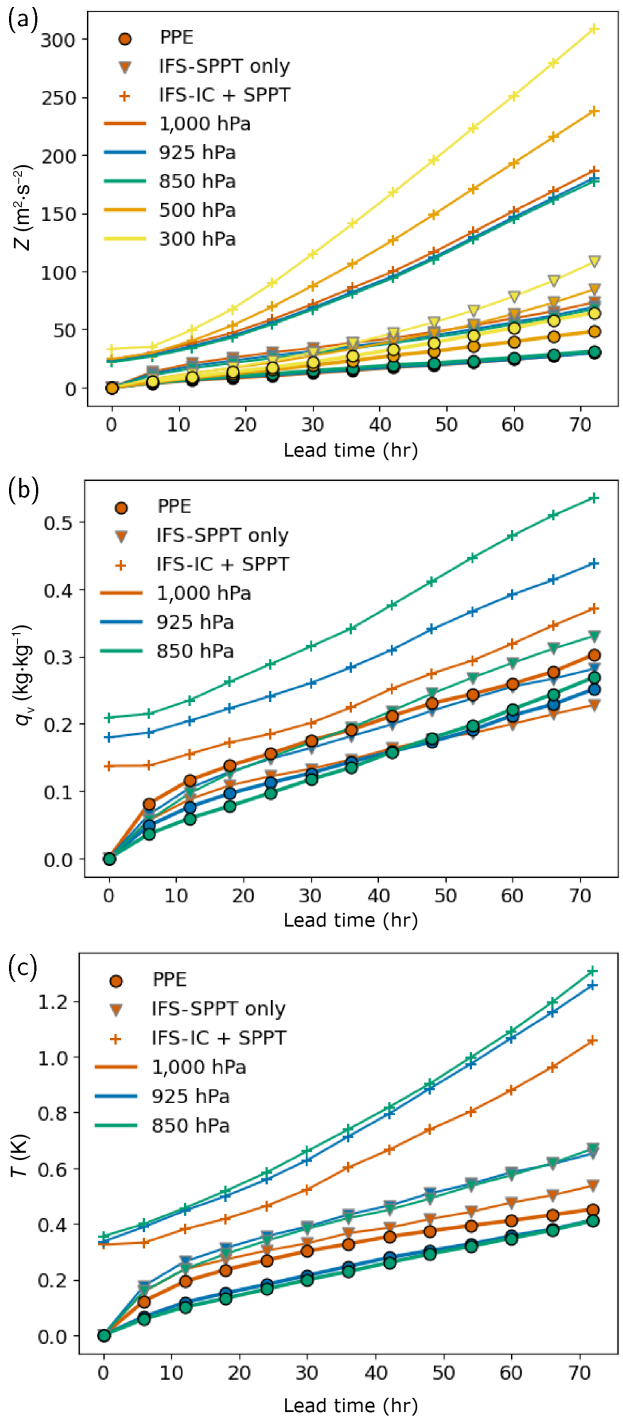

FIGURE 5 Ensemble spread per lead time in the 50-member training perturbed parameter ensemble (PPE; circles), and compared with 21-member Integrated Forecasting System (IFS) simulations run with stochastically perturbed parametrisation tendencies (SPPT) only ("IFS-SPPT only"; triangles) and run with SPPT and initial condition (IC) perturbation ("IFS-IC+SPPT"; crosses). The spread is spatially averaged across −50 to −5°E and 35–75°N. (a) Geopotential Z ($m^2 \cdot s^{-2}$), (b) specific humidity q_v (kg·, kg^{-1}), and (c) temperature T (K). The IFS ensemble is initialised 6 hr later than the ICON PPE. IFS ICs perturbations create spread already at the initial lead time in "IFS-IC+SPPT".

members are characterised by potentially unstable conditions (i.e., $d\theta_e/dz < 0\ K \cdot m^{-1}$) in the lowest 1.5 km over the ocean surface (not shown). The vertical redistribution of higher temperature and moisture content with warmer SST leads to systematically stronger potential instability, and the depth of the potentially unstable layer is slightly extended. The lower tropospheric WCB inflow region is thus characterised by enhanced temperature and moisture availability, as well as slightly decreased static stability and enhanced potential instability when SST is warmed.

From the comparison of the ensemble spread, we conclude that the choice of parameter perturbation ranges is reasonable; that is, the combined perturbations induce substantial spread that is also projected to the larger scale—albeit more slowly than in the operational IFS ensemble with a very different perturbation design. At the same time, the PPE members are still reasonably representing the synoptic situation and do not entirely diverge from the reference simulation. The projection of small-scale perturbations to the large-scale flow is relevant in the error growth framework (Baumgart *et al.*, 2019; Zhang *et al.*, 2007), as small-scale errors near the waveguide can be amplified through dry dynamic Rossby wave amplification.

In the following, we discuss how the perturbations influence WCB ascent (Section 4), which propagates cloud microphysical perturbations from the smaller to the larger scale and SST perturbations from the surface to the upper troposphere. In Sections 5 and 6, we illustrate which perturbations most strongly influence precipitation characteristics and the larger scale flow.

4 | INFLUENCE OF PARAMETER PERTURBATIONS ON WCB ASCENT

The parameter perturbations influence the WCB ascent in many different ways. In the following, we discuss the perturbation impact on the WCB ascent in detail (Section 4.1) before quantifying dominant sources of uncertainty for the observed changes in WCB characteristics (Section 4.2), focusing specifically on WCB air mass transport and ascent time-scales, total ascent integrated diabatic heating, and local diabatic heating and ascent velocity maxima along the ascent (see Table 3).

4.1 | WCB ascent characteristics

As exemplified in Section 2.3, the number of WCB trajectories N_{tra}—that is, the number of trajectories fulfilling the criterion of at least 600 hPa ascent in 48 hr— which is a proxy for air mass transport from the lower into

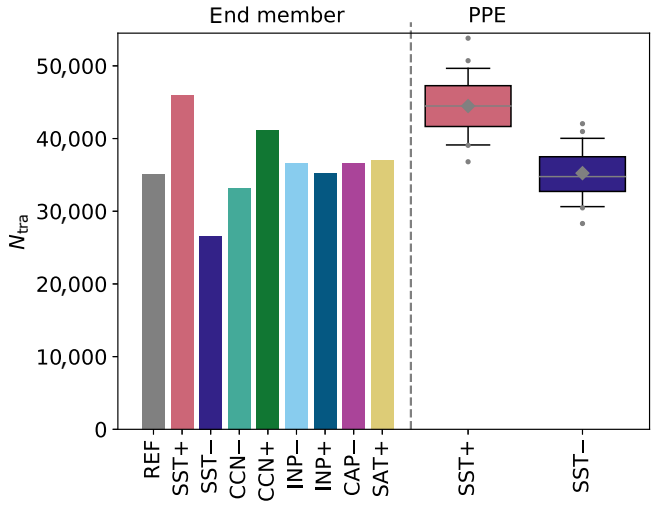

FIGURE 6 Number of warm conveyor belt trajectories in the individual end members. Red and blue boxplots respectively show perturbed parameter ensemble (PPE) members with positive and negative sea-surface temperature (SST) perturbations. Shown are median (grey line), mean (grey marker), and outliers exceeding the 5th and 95th percentiles (grey points). The whiskers denote the 5th and 95th percentile range. CCN: cloud condensation nuclei concentration; INP: ice nucleating particle concentration; CAP: capacitance of snow and ice; SAT: supersaturation with respect to liquid.

the upper troposphere, varies across the individual simulations (Figure 6). N_{tra} across all PPE members varies between 28,000 and 54,000. On average, N_{tra} is larger in the members with positive SST perturbations (Figure 6). Among all end members, the largest influence on N_{tra} results from changes of SST, although CCN perturbations to a smaller extent also change N_{tra} (Figure 6). The individual perturbations of INP, SAT, and CAP only lead to minor N_{tra} changes. These results are consistent with Figure 3f and will be discussed further in Section 4.2.

The larger N_{tra} for warmer SST conditions results to some extent from the poleward expansion of the WCB inflow and ascent region. Figure 7a shows the track of the centre of mass of the WCB inflow position for both SST end members and the unperturbed reference, which illustrates the more poleward orientation of the WCB inflow position with increased SST. Close to the initialisation time of the simulation, WCB air parcels originate from the same region, whereas the mean region of origin drifts further apart with increased lead time and results in a more poleward-directed mean track with warmer SST. Figure 7b illustrates the systematic poleward expansion of the WCB origin region with increased SST for both end members, whereby the southern edge of the WCB origin region is hardly modified. Specific humidity in the WCB inflow averaged over all WCB trajectories does not differ strongly between the SST end members, or across the individual PPE members (not shown). This is a direct result of the poleward expansion (and not poleward shift) of the region of origin; that is, incorporation of air masses climatologically characterised by lower temperature, and thus lower specific humidity, into the WCB inflow (Figure 7b). However, at a given latitude, the specific humidity content (Figure 7b) and temperature (not shown), and thus equivalent potential temperature θ_e, of WCB inflow is higher when SST is increased. This gives rise to increased latent heat release and stronger cross-isentropic ascent. As a result, air parcels farther poleward also realise a deep ascent of 600 hPa, which extends the WCB ascent region further poleward and shifts the mean WCB inflow positions with increasing SST (Figure 7a).

In addition to an increase in N_{tra} and poleward extension of the WCB origin and ascent regions with increasing SST, the detailed WCB ascent behaviour is substantially influenced by the parameter perturbations. The distributions of the time-scale for WCB ascent τ_{600}, defined as the minimum time required to ascend 600 hPa, is shifted to shorter time-scales with warmer SST across the PPE (Figure 8). Mean τ_{600} is reduced and, in particular, τ_{600} values below 25 hr occur more frequently. In contrast, the frequency of more gradual and slantwise WCB trajectories, characterised by ascent time-scales of more than 30 hr, is hardly influenced by the perturbations. Hence, the parameter perturbations more strongly influence the fraction of faster ascending WCB trajectories. Very rapid and convective ascent, with τ_{600} values below 3–4 hr, also occurs more frequently in warmer SST conditions. Lifting of the potentially unstable air ahead of the cold front favours convective ascent embedded in the WCB ascent region (Oertel *et al.*, 2020). We hypothesise that the increase of potential instability through increasing SST favours enhanced convective ascent. However, the high correlation (> 0.99) between low-level temperature and stability hinders the disentangling of the effect of stability versus θ_e.

To summarise, taking N_{tra} as proxy for air mass transport from the lower into the uppermost troposphere, increased SST leads to enhanced air mass transport. This is consistent with other WCB cases that have shown sensitivity to the underlying SST (Christ *et al.*, 2025). The increase in N_{tra} partially results from the poleward extension of the WCB inflow and ascent region, given an increase in θ_e in these regions resulting from enhanced surface fluxes. Moreover, warmer SST is associated with faster ascent; that is, shorter ascent time-scales, and in particular a larger number of very rapidly ascending WCB trajectories. Though changes in absolute SST directly impact surface fluxes, the influence of SST on surface fluxes can be further strengthened by feedback with cyclone dynamics. An initial increase of surface latent heat flux can

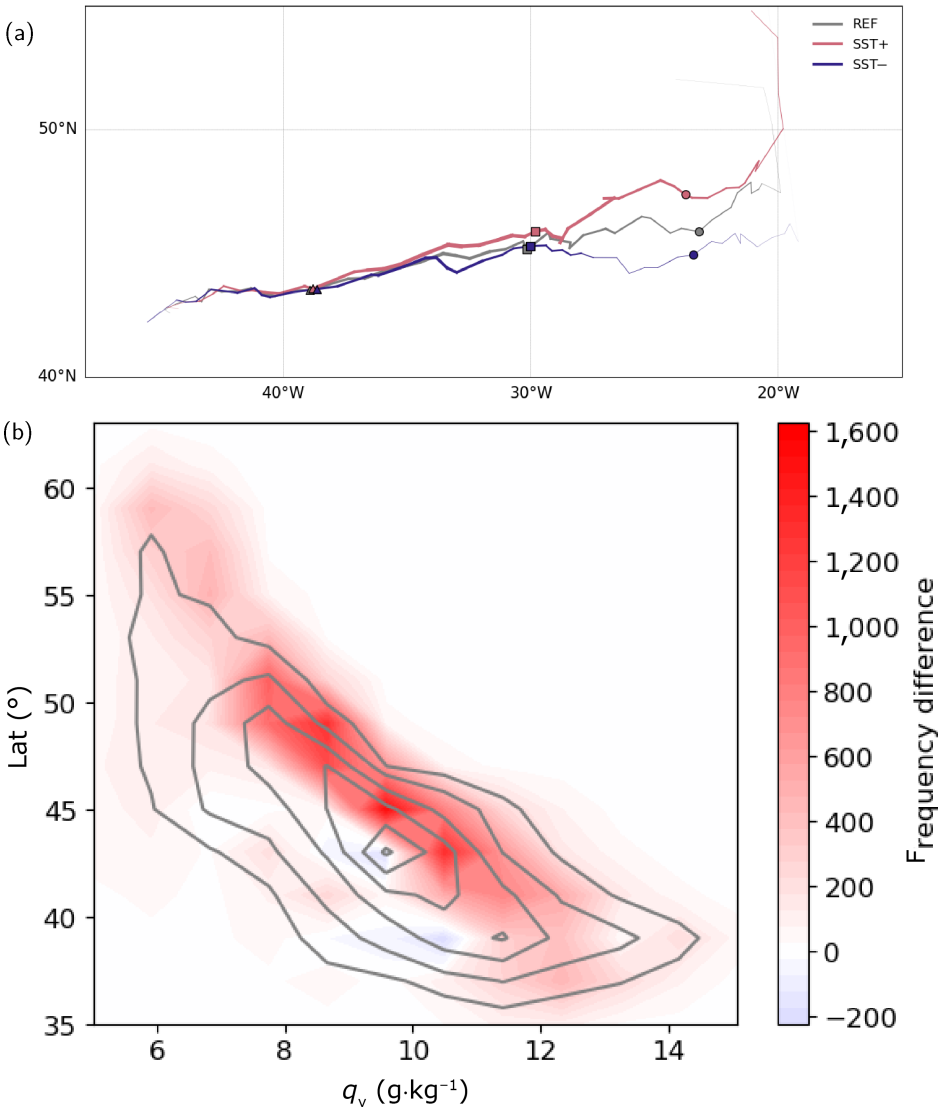

FIGURE 7 (a) Evolution of mean warm conveyor belt (WCB) inflow region (longitude and latitude at start of ascent) during first 48 hr lead time for the simulations with maximum perturbations of sea-surface temperature (SST) only (red: SST + 2 K; blue: SST − 2 K). The line width is proportional to the number of WCB trajectories. The coloured markers indicate the positions at 12 hr (triangle), 24 hr (square), and 36 hr (circle) lead time. (b) Two-dimensional distribution of WCB inflow latitude (lat, °) and specific humidity q_v (g · kg^{-1}) for the unperturbed reference member (grey contours). Red and blue shading shows the frequency difference between SST + 2 K and SST − 2 K end members.

slightly increase cyclone strength through enhanced diabatic heating (Binder *et al.*, 2016; Christ *et al.*, 2025), and the associated increase in near-surface wind speeds may further strengthen surface fluxes. The contribution of the cloud microphysical perturbations to changes in the WCB ascent characteristics relative to the impact of SST will be quantified in Section 4.2.

The detailed analysis of diabatic heating and vertical velocity along WCB trajectories provides more insight into the influence of microphysical heating on WCB ascent velocity, as well as the impact of parameter perturbations. Figure 9a,b shows 1-hr integrated diabatic heating $\Delta\theta$ and 1-hr mean vertical velocity w along WCB trajectory ascent stratified into 2 K temperature bins following the ascent averaged over all WCB trajectories per PPE member. Stratification into temperature bins, instead of commonly used pressure bins, emphasises the coherent diabatic heating structures dominated by individual cloud microphysical processes that are more directly influenced by temperature than pressure. The shapes of the quasi-vertical Lagrangian profiles of w and $\Delta\theta$ are (surprisingly) similar (Figure 9a,b), which emphasises the strong correlation between latent heat release, primarily from cloud microphysical heating, and vertical velocity of WCB air parcels. Both profiles are characterised by two local maxima each: one in the warm-phase region and one in the cold-phase or mixed-phase region above the melting level (Figure 9a,b). The warm-phase and cold-phase maxima in $\Delta\theta$ respectively arise to a large extent from latent heat release from condensational growth of cloud droplets (realised by the first saturation adjustment; dark red line in Figure 9c) and deposition of vapour onto frozen hydrometeors (pink line in Figure 9c). Both maxima are separated by a local minimum in $\Delta\theta$ and w, which coincides with the melting level at 273 K and the maximum of cooling from melting of sedimenting frozen hydrometeors (green line in Figure 9c). The locally reduced total diabatic heating from melting locally reduces the vertical

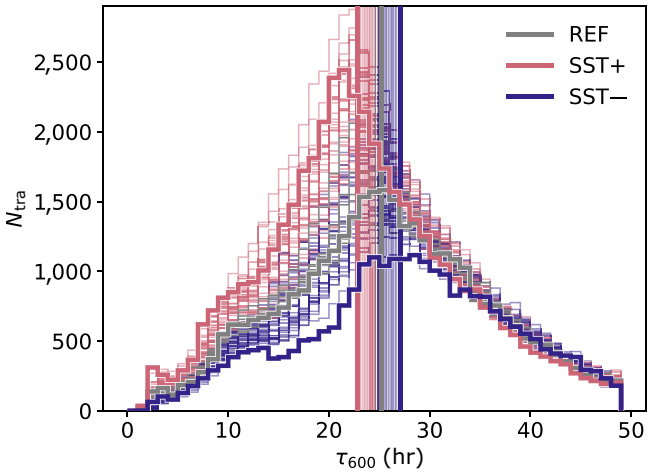

FIGURE 8 Histograms of time-scale for warm conveyor belt ascent τ_{600} (hr). Red and blue colours respectively show distributions for members with positive and negative sea-surface temperature (SST) perturbations. The highlighted distributions show the unperturbed reference (grey), and the end members with +2 K and −2 K perturbations to SST. The vertical lines show the respective mean values of τ_{600}.

velocity during WCB ascent, indicating that latent heat release modulates vertical velocity. At the warmest temperature, averaged vertical velocity is slightly negative, as trajectories descend slightly before their main ascent (Figure 9b). In the upper troposphere, both $\Delta\theta$ and w decrease as the WCB air parcels finish their ascent. The vertical profile of the liquid fraction (Figure 9d) illustrates that the liquid fraction decreases rapidly with decreasing temperature, although the mixed-phase region in the WCB can extend to temperatures just below 240 K.

PPE members with high SST (Figure 9a,b; red line) are characterised by larger maximum $\Delta\theta$ in the warm-phase region and a larger maximum $\Delta\theta$ in the mixed-phase region, which manifests in larger 1-hr w throughout the entire ascent. For colder SST (Figure 9a,b; blue line), the effect is reversed; that is, diabatic heating and the vertical velocity are reduced. The variability of the maximum $\Delta\theta$ in the mixed phase is, however, not only strongly influenced by SST perturbations. In contrast, the smallest diabatic heating rates in the mixed phase near the $\Delta\theta$ maximum occur in the simulations where CAP is reduced (Figure 9a; purple line); that is, where the mass growth rate of frozen hydrometeors through vapour deposition is lower. The reduction of vapour deposition leads to an even stronger reduction of total $\Delta\theta$ than the decrease of SST does. This is also directly imprinted in the vertical velocity (Figure 9b; purple line), which is substantially reduced as a result from reduced diabatic heating, confirming from a model perspective the observation-based hypothesis by von Terzi *et al.* (2022) that increased enhanced depositional growth in the dendritic growth layer around 260 K locally increases vertical velocity (see also Schrom & Kumjian, 2016). A reduction of CAP also leads to a vertical displacement of the diabatic heating profile from vapour deposition, such that $\Delta\theta$ (and w) are larger at temperatures below 250 K for low CAP members, because the heating is delayed along the ascent. Thus, enhanced vertical velocity can be sustained in colder temperatures at higher altitudes. The feedback between CAP and $\Delta\theta$ (as well as w) is primarily relevant during the transition to a fully glaciated cloud; that is, when latent heating is less thermodynamically constrained by the saturation adjustment.

We conclude that the WCB ascent velocity in the cold-phase region is directly influenced by latent heat release from cloud formation, that is, the detailed representation of cloud microphysical process rates locally influences the ascent strength of the ascending WCB air parcels. In the following, we quantify the contributions of the individual perturbed parameters to the total variance in WCB ascent behaviour and diabatic heating to disentangle the different sources of uncertainty.

4.2 | Quantification of uncertainty contributions for WCB ascent characteristics

The parameter impacts on the general WCB ascent behaviour described in Section 4.1 can be summarised by changes in N_{tra}, mean τ_{600}, and the fraction of rapidly ascending trajectories with 600 hPa ascent times below 3 hr and 10 hr (f_{3h} and f_{10h} respectively; Figures 6 and 8). Following the method illustrated earlier for N_{tra} (Sections 2.3 and 2.4), we develop statistical surrogate models independently for these target variables using Gaussian process emulation and perform variance-based sensitivity analysis.

Consistent with the mean modulation of N_{tra} by SST (Figure 6), the variance decomposition shows that SST explains the largest percentage of variance in N_{tra}, with only small contributions from CCN and INP (Figure 10). Extending this analysis to τ_{600} confirms the qualitative conclusions from Section 4.1, suggesting that SST also most strongly contributes to the variance in τ_{600} (Figures 8 and 10). Thus, the air mass transport into the upper troposphere and the WCB ascent time-scales are most strongly influenced by SST, whereas the changes in cloud microphysical parameters have a comparably small contribution. This also applies to the fraction of fast WCB trajectories with τ_{600} values below 10 hr (f_{10h}). Here, the main effect of SST represents more than 80% of the variance. The fraction of convectively ascending WCB

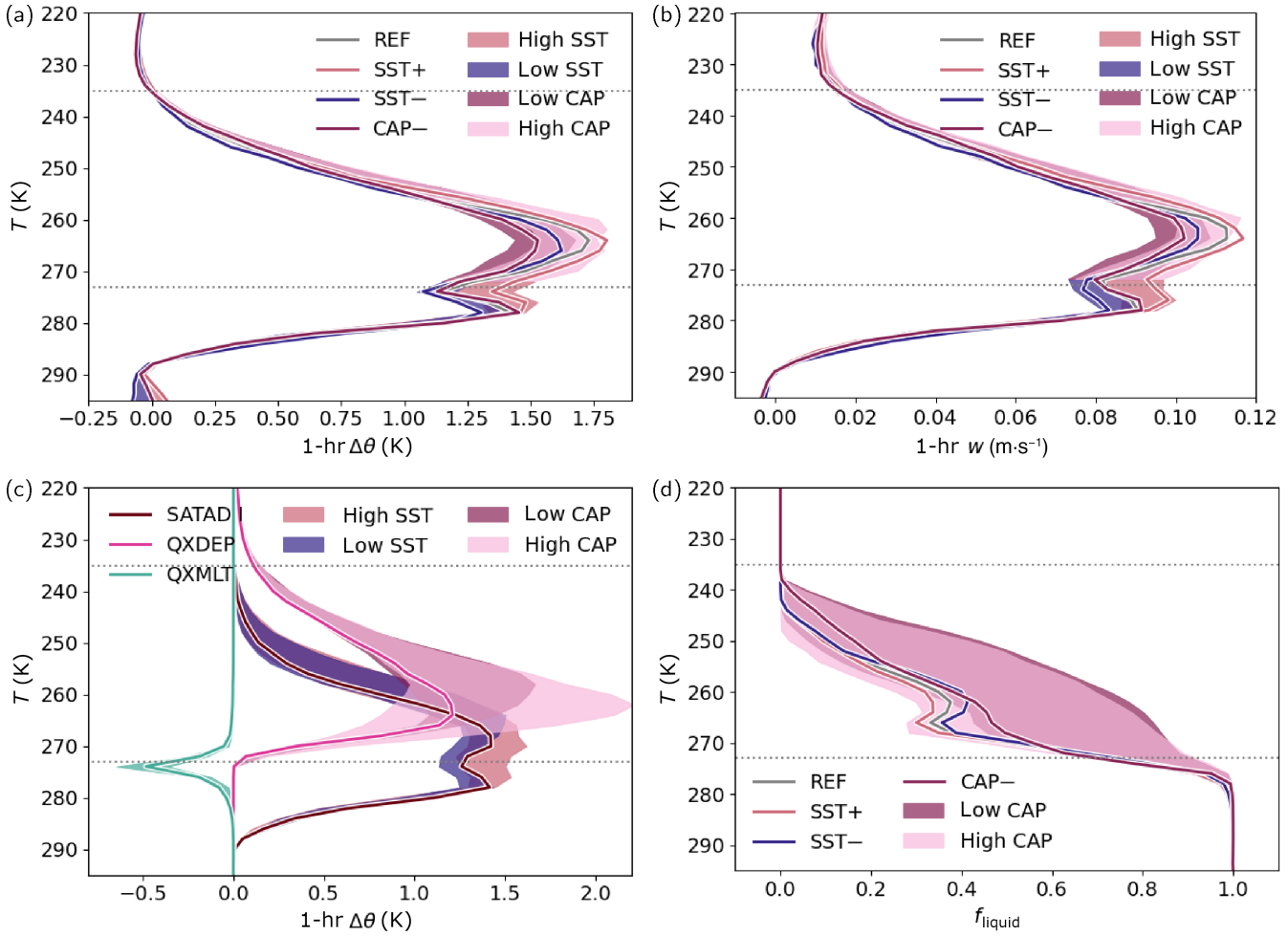

FIGURE 9 (a, c) The 1-hr diabatic heating $\Delta\theta$ (K), (b) 1-hr mean vertical velocity w ($\mathrm{m \cdot s^{-1}}$), and (d) mean liquid fraction f_{liquid} along warm conveyor belt trajectories for individual ensemble members in temperature bins. The dashed lines show the 0°C isotherm and the −38°C isotherm. (a) Total $\Delta\theta$ with the respective envelopes from all perturbed parameter ensemble (PPE) members. In the warm phase ($T > 273$ K), PPE members are stratified according to their sea-surface temperature (SST) perturbations (blue envelope: SST < 0 K; red envelope: SST > 0 K). In the cold phase ($T < 273$ K), PPE members are stratified according to their capacitance (CAP) perturbations (purple envelope: CAP < 0.6; pink envelope: CAP > 0.6). Four selected end members are highlighted in bold (grey: REF; blue: SST− (−2 K); red: SST+ (+2 K); purple: CAP− (CAP = 0.2). (b) As (a) but for w. (c) $\Delta\theta$ from the first saturation adjustment (SATAD), depositional growth of frozen hydrometeors (QXDEP), and melting of frozen hydrometeors (QXMLT) from the unperturbed reference simulation. Additionally, the respective envelopes from all PPE members are shown, whereby SATAD is stratified according to SST perturbations (blue envelope: SST < 0 K; red envelope: SST > 0 K) and QXDEP is stratified according to CAP perturbations (purple envelope: CAP < 0.6; pink envelope: CAP > 0.6). (d) f_{liquid} is stratified according to CAP perturbations (purple envelope: CAP < 0.6; pink envelope: CAP > 0.6).

trajectories ($f_{3\mathrm{h}}$) is noticeably influenced by SAT (ME = 16%), in addition to SST (ME = 76%), which is thus still the major source of uncertainty (Figure 10). The increase of maximum SAT during the ascent reduces diabatic heating from condensational growth of cloud droplets, which feeds back on the vertical velocity. In particular, the rapidly ascending trajectories are heated most strongly by condensational growth in the lower troposphere. As a result, facilitating larger SAT in the saturation adjustment scheme to some extent reduces the major diabatic heating source of the fastest trajectories, and thus the fraction of convectively ascending trajectories. Owing to the scaling of maximum supersaturation with w, Equation (2), the effect is strongest for the most rapidly ascending trajectories. The large variability in N_{tra} across the PPE also substantially influences the total WCB-related diabatic heating (Figure 10), defined as the sum of 600 hPa ascent-integrated diabatic heating (ADH_{600}) over all WCB trajectories ($\sum_{i=1}^{N_{\mathrm{tra}}} \mathrm{ADH}_{600,i}$). As N_{tra} is most strongly influenced by SST, the variance in the total WCB-integrated diabatic heating is also most strongly influenced by SST, and intuitively warmer SST results in enhanced heat transport into the uppermost troposphere by the WCB.

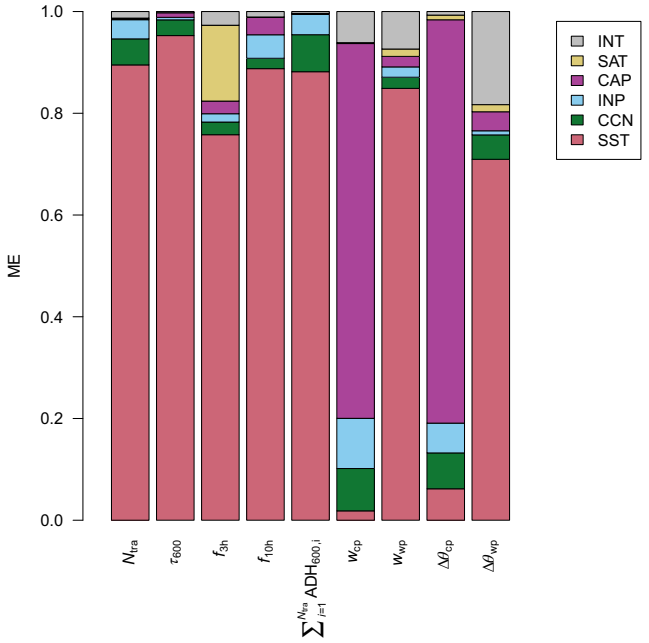

FIGURE 10 Main effects (MEs) for number of trajectories N_{tra}, mean ascent time-scale τ_{600}, fraction of trajectories with $\tau_{600} < 3$ hr and $\tau_{600} < 10$ hr, total warm conveyor belt (WCB)-integrated diabatic heating $\sum_{i=1}^{N_{tra}} ADH_{600,i}$, and maximum of 1-hr mean vertical velocity w and 1-hr diabatic heating $\Delta\theta$ of WCB trajectories for the cold phase (cp; $T < 273$ K) and warm phase (wp; $T > 273$ K). The grey colour represents the contributions from parameter interactions (INT). SST: sea-surface temperature; CCN: cloud condensation nuclei concentration; INP: ice nucleating particle concentration; CAP: capacitance of snow and ice; SAT: supersaturation with respect to liquid.

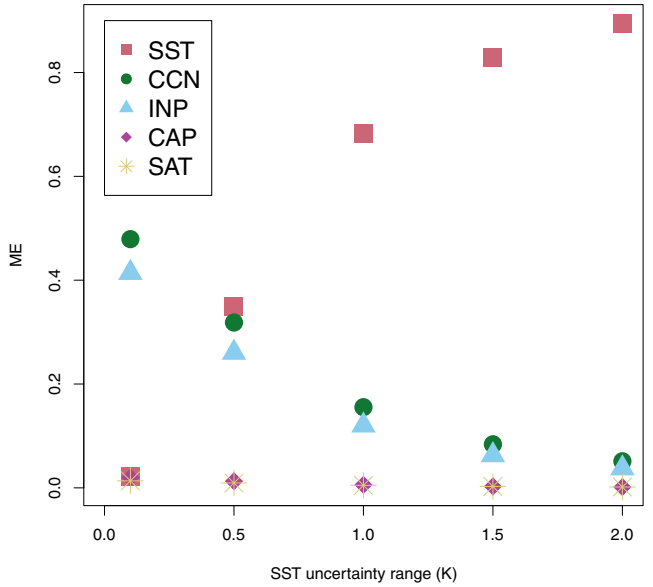

FIGURE 11 Main effects (MEs) for emulator predictions as in Figure 3 with gradually decreasing range of sea-surface temperature (SST) variability used in the variance decomposition. The numbers of perturbed parameter ensemble members in each SST range amount to 70 for ±2 K, 52 for ±1.5 K, 34 for ±1.0 K., 18 for ±0.5 K, and 4 for ±0.1 K. CCN: cloud condensation nuclei concentration; INP: ice nucleating particle concentration; CAP: capacitance of snow and ice; SAT: supersaturation with respect to liquid.

The detailed temperature-resolved diabatic heating and vertical velocity rates along the ascent are influenced by both SST and CAP, as illustrated in Figure 9a,b. The variance decomposition provides more details on the dominant sources of uncertainty and also includes the impacts of CCN, INP, and SAT. To describe the variability in the Lagrangian profiles shown in Figure 9a,b we develop Gaussian processes to predict the amplitude of both local maxima of 1-hr $\Delta\theta$ and 1-hr w. The maxima of 1-hr $\Delta\theta$ and 1-hr w in the cold phase (i.e., at temperatures below 273 K), $\Delta\theta_{cp}$ and w_{cp}, are most strongly influenced by CAP (ME > 70%). As mentioned earlier, the feedback of a reduction of CAP on vertical velocity in the cold phase demonstrates that diabatic heating from depositional growth influences local vertical velocity (Schrom & Kumjian, 2016; von Terzi *et al.*, 2022). A total of 10–20% of the variance is also explained by changes to CCN and INP, which additionally influence diabatic heating in the upper troposphere. The impact of SST on the vertical velocity maximum in the cold phase is relatively small. In contrast, more than 85% of the variance in warm-phase maximum w (w_{wp}) is influenced by SST, and the main effect of SST for the warm-phase diabatic heating maximum ($\Delta\theta_{wp}$) amounts to 71%. For $\Delta\theta_{wp}$, the sum of all individual main effects accounts only for 82% of the variance, indicating that the diabatic heating maximum is additionally influenced by the interactions between the individual parameters. This suggests that for $\Delta\theta_{wp}$ not only the underlying SST is important, but parameter combinations result in nonlinear changes in $\Delta\theta_{wp}$ that cannot be captured by one-at-a-time parameter perturbations.

4.3 | Influence of reduction of SST uncertainty range

The relative parameter influence depends directly on the predefined ranges of the parameter perturbations. Although the range of SST perturbations introduces specific humidity biases well within the range of observations (Schäfler & Harnisch, 2015), the absolute values of the upper and lower limits are uncertain. To evaluate the dependency of the relative importance of SST perturbations on the predefined SST range, we reduce the SST range gradually from ±2 K to ±0.1 K for the variance-based sensitivity analysis exemplary for the target variable N_{tra} (Figure 11 and Supporting Information Figure A1). The

variance decomposition suggests that SST remains the dominant driver of uncertainty for N_{tra} for perturbation ranges larger than ±1 K (Figure 11). Only when the SST uncertainty range decreases below ±0.5 K do the relative contributions of CCN and INP become almost equally important as the contributions from SST perturbations. Although the emulator is based on the full 50 training PPE members, only 18 PPE members are within the SST range of ±0.5 K, which may lead to some uncertainty in the estimation of individual parameter uncertainty if the response surface between individual parameters was not sufficiently smooth and not adequately represented by the emulator. Overall, this corroborates the important role of absolute SST for WCB ascent by increasing WCB inflow specific humidity, temperature, and potential instability. Yet, CCN and INP perturbations also systematically influence WCB ascent, although their impact on WCB ascent, specifically N_{tra}, is substantially smaller than the applied SST perturbations are (see also Figure 6). Once SST perturbations are removed (Figure 11 and Supporting Information Figure A1), CCN and INP are the dominant sources of uncertainty, whereby CCN and INP are respectively positively and negatively correlated with N_{tra}.

In summary, uncertainty in the WCB ascent characteristics results primarily from variability in the prescribed SST, although the detailed representation of cloud microphysical processes additionally contributes to uncertainty in the detailed ascent behaviour. The larger sensible and latent heat fluxes, which are primarily caused by warmer SST, warm, moisten, and destabilise the lower troposphere. The ascending WCB efficiently feeds on the additional heat and moisture source, whereby diabatic heating from enhanced cloud formation determines the cross-isentropic ascent and influences the detailed WCB ascent behaviour. In particular, in the cold phase, cloud microphysical processes have a dominant influence on local vertical velocity along the ascending airstream.

5 | PARAMETER IMPACT ON PRECIPITATION CHARACTERISTICS

In the following, we quantify the parameter impact on NWP forecast properties, starting with surface precipitation characteristics and continuing with the large-scale upper level flow pattern (Section 6).

To understand how the parameter perturbations influence precipitation formation and surface precipitation characteristics, we consider both Eulerian and Lagrangian perspectives, and specifically analyse time and domain mean surface precipitation sums (Section 5.1), cloud microphysical precipitation efficiencies (Section 5.2), and precipitation intensities and their spatial distribution (Section 5.3).

5.1 | Integrated surface precipitation

The surface precipitation in the North Atlantic during the case study period is primarily associated with WCB ascent (Figure 1a,c,e). The total hourly surface precipitation sums are highest during October 4 and decrease on October 5 toward October 6 (Figure 12a) as the WCB airstream moves poleward and the ascending motion weakens (cf. Figure 7a). The temporal evolution of hourly surface precipitation across the individual PPE members is very similar (Figure 12a), but generally members with positive SST perturbations have larger surface precipitation amounts, which is consistent with more pronounced WCB ascent and higher surface fluxes in high SST scenarios. For each PPE member, the total area-integrated surface precipitation sum is calculated and integrated over the first 24 hr ($P_{sfc,24h}$), 36 hr ($P_{sfc,36h}$), 48 hr ($P_{sfc,48h}$), and 72 hr ($P_{sfc,72h}$) lead time of the simulation. To remove effects from model spin-up, the first 3 hr lead time are always excluded. The precipitation is only considered in a box confined to the major WCB ascent region, which extends from −55 to −14°E and 35–75°N to minimise effects from non-WCB-related precipitating systems. For the time- and domain-integrated precipitation sums, Gaussian process emulators were trained for each of the integration times (Supporting Information Figures A2–A5). The parameter influence on the respective surface precipitation sums is summarised in Figure 13.

As expected from the sensitivity of WCB ascent behaviour to SST, warmer SST is associated with increased surface precipitation related to generally enhanced ascending motion (Figure 8) and increased moisture availability in the inflow region (Figure 7b and Supporting Information Figure A6). The variance of surface precipitation sums at shorter integration times of 24 hr and 36 hr is additionally influenced by cloud microphysical parameters, especially CCN and CAP, which influence hydrometeor growth rates and therefore efficiency of precipitation formation. The contributions of CCN and CAP to the variance of the time- and domain-integrated precipitation sums gradually decreases as the integration time increases (Figure 13). For an integration time of 72 hr, which approximately covers the life cycle of this WCB case, almost all the variance in surface precipitation is explained by SST, which is almost linearly related to the precipitation sum (Supporting Information Figure A2). The 72-hr integrated surface precipitation sums in the PPE members vary by up to ±8% compared with the unperturbed reference. Thus, during the life cycle of the

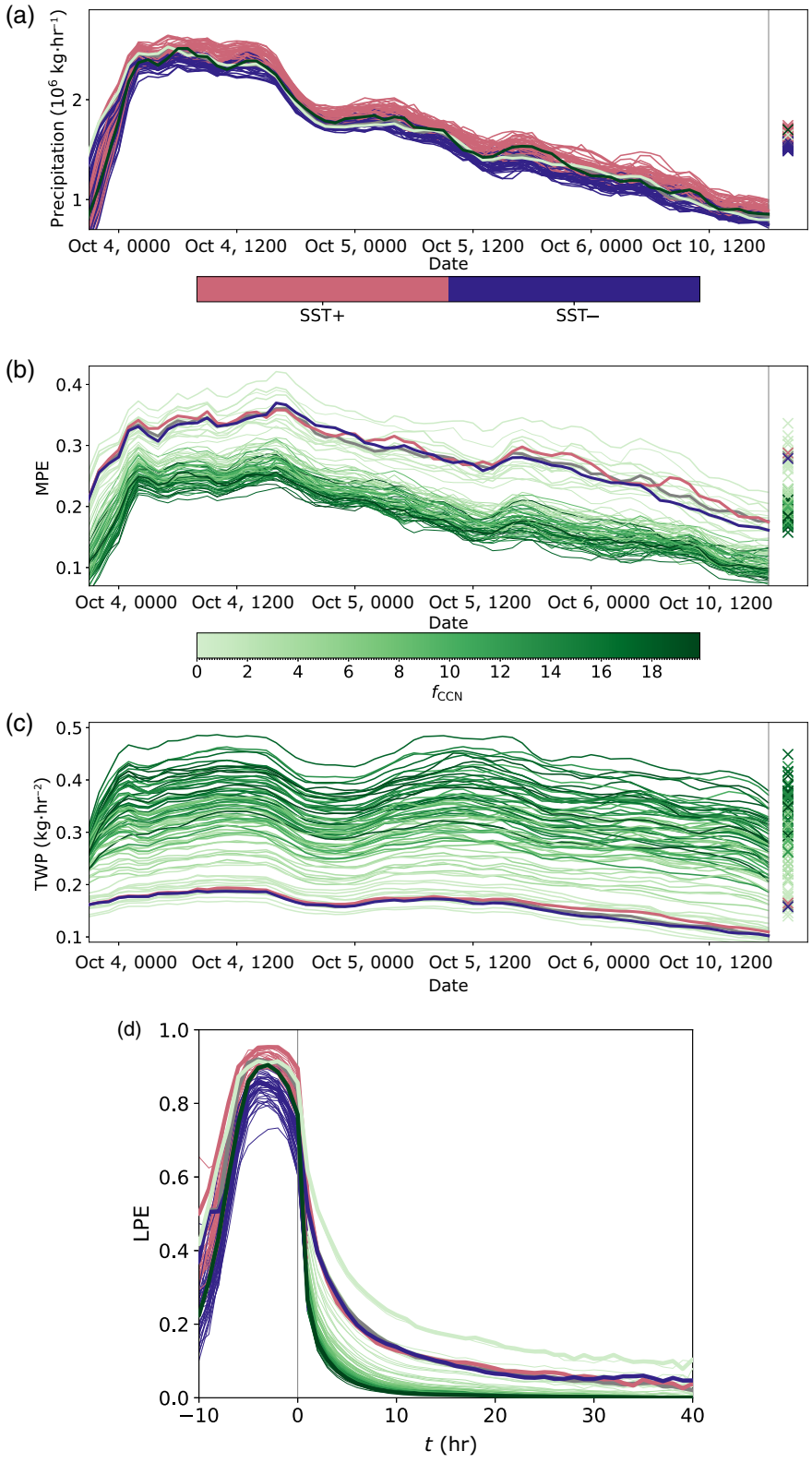

FIGURE 12 (a) Evolution of hourly precipitation sums in the North Atlantic region (−55°E to −14°E, 35°N to 75°N) for all perturbed parameter ensemble (PPE) members plus end members. Each member is coloured according to their sea-surface temperature (SST) perturbation, except for the cloud condensation nuclei (CCN) end members and the reference, which are coloured in green and grey respectively. The markers denote the temporal mean. (b) Evolution of hourly microphysical precipitation efficiency (MPE) in the North Atlantic region for all PPE members plus end members coloured according to their CCN perturbation, except for the two SST end members and the reference, which are coloured in red, blue and grey respectively. The markers denote the temporal mean used for Gaussian process emulation. (c) As (b) but for spatially averaged total water path (TWP, kg · m^{-2}). (d) Lagrangian precipitation efficiency (LPE), defined as rain mass fraction, $q_r/(q_r + q_c)$, along ascending warm conveyor belt trajectories for all PPE members plus end members coloured according to their CCN perturbation except for the two SST end members and the reference, which are coloured in red, blue and grey respectively.

WCB, the available moisture in the WCB inflow substantially impacts total precipitation during subsequent ascent, whereas at shorter integration times the precipitation efficiency influences the time and domain sums. This suggests that the ascending WCB airstream efficiently transports the available low-level humidity upward, which finally results in larger time- and domain-integrated surface precipitation sums if SST is increased. We conclude that the moisture availability in the WCB inflow, influenced by the effect of SST on latent heat fluxes, is a primary

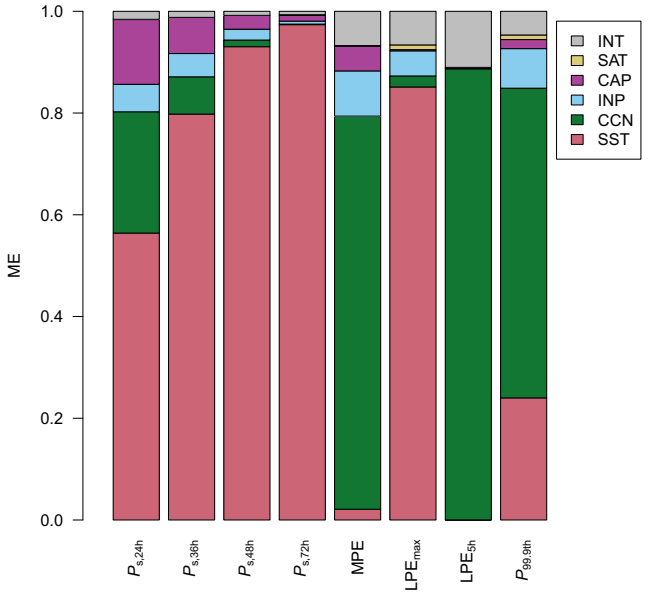

FIGURE 13 Main effects (MEs) for time- and domain-integrated precipitation sums integrated over different lead times of 24, 36, 48, and 72 hr, microphysical precipitation efficiency (MPE), the maximum of Lagrangian precipitation efficiency prior to warm conveyor belt ascent (LPE_{max}), LPE after 5 hr (LPE_{5h}), and the frequency of intense surface precipitation (exceedance of 99.9th percentile of the unperturbed reference simulation, $P_{99.9th}$). The grey colour represents the contributions from parameter interactions (INT). SST: sea-surface temperature; INP: ice nucleating particle concentration; CAP: capacitance of snow and ice; CCN: cloud concentration nucleus; SAT: supersaturation with respect to liquid.

source of uncertainty for WCB-related precipitation sums on longer integration time-scales. Yet, detailed representation of precipitation efficiency and hydrometeor growth rates becomes more important if shorter time-scales are considered. For example, emulation of $P_{sfc,24h}$ shows that an increase in CCN concentration and a reduction of the strength of vapour deposition (CAP) decrease surface precipitation sums on a time-scale of 24 hr, and together contribute about 40% to the total variance (Figure 13). In next Section 5.2 we elaborate on the impacts on precipitation efficiency that can delay precipitation formation for several hours.

5.2 | Precipitation efficiency

Precipitation efficiency describes how efficiently cloud condensate is converted to surface precipitation. We disentangle the parameter influence on precipitation efficiency from two complementary perspectives, a Lagrangian and Eulerian approximation of precipitation efficiency, which are outlined in the following.

1. *Cloud microphysical precipitation efficiency* We first approximate the cloud microphysical precipitation efficiency (MPE), Equation (5) (e.g., Sui *et al.*, 2007), defined as the ratio of domain-integrated surface precipitation P_{sfc} to the vertically integrated sum of vapour deposition and condensation rates. Hence, MPE specifies how efficient cloud condensate formed by particle nucleation, vapour deposition, and condensation is converted to precipitation-sized particles and reaches the surface. As ICON uses two saturation adjustments, the estimation of MPE in ICON needs to consider the partially counteracting effects of the second saturation adjustment (SATAD2), which strongly influences the hydrometeor and specific humidity budget; see Oertel *et al.* (2023a) for more details. In the mixed-phase region at a temperature below 273 K, vapour deposition on frozen hydrometeors (QXDEP) causes subsaturation with respect to liquid. This subsaturation is compensated by the second saturation adjustment, which is called after the explicit cloud microphysical processes and which evaporates cloud droplets until critical saturation specific humidity $q*_{v,s}(T,p)$ is again established. This growth of frozen hydrometeors at the expense of cloud droplets (i.e., the Wegener–Bergeron–Findeisen process; Storelvmo & Tan, 2015) needs to be considered for the approximation of MPE in ICON. To account for this quasi-compensation, the mass growth rates from the second saturation adjustment and vapour deposition are summed up prior to their vertical integration over all net positive contributions. We approximate MPE as follows:

$$\mathrm{MPE} = \frac{P_{sfc}}{[\mathrm{SATAD}] + [(\mathrm{SATAD2} + \mathrm{QXDEP})]}. \quad (5)$$

Square brackets denote a vertically integrated quantity. Prior to vertical integration, negative process rates, which indicate a loss of hydrometeor mass through evaporation or sublimation, are removed. Note that the feedback between the second saturation adjustment and the turbulence scheme in ICON in the warm-phase and mixed-phase regions can introduce some uncertainties in the approximation of MPE; see Oertel *et al.* (2023a) for details. MPE is calculated hourly from 1-hr P_{sfc} sums and 1-hr instantaneous condensation (SATAD and SATAD2) and vapour deposition (QXDEP) rates, which were added up in the box confined to the major WCB ascent region (−55°E to −15°E and 35°N–55°N). As this area is relatively large, we assume that advective fluxes of cloud condensate into and out of the region are negligible.

2. *Lagrangian (warm-phase) precipitation efficiency* We define a Lagrangian precipitation efficiency (LPE) as the ratio of rainwater content to the sum of rain and cloud water content along the ascending WCB trajectories, Equation (6). To analyse the evolution of mean LPE along the ascent, WCB trajectories are centred relative to the start of their fastest 600 hPa ascent period ($t = 0$ hr). LPE is primarily meaningful to quantify the effects of CCN and SST in the early phase of WCB ascent when the frozen fraction is small. It provides a suitable WCB-centred perspective to understand how the parameter perturbations influence (warm-phase) precipitation formation along the ascent and disregards effects from non-WCB-related clouds.

$$\mathrm{LPE} = \frac{q_\mathrm{r}}{q_\mathrm{r} + q_\mathrm{c}}. \tag{6}$$

The Eulerian MPE overall varies between 15% and 40% (Figure 12b). In all PPE members, MPE decreases with increasing lead time and concomitant weakening of WCB ascent, cloud formation, and total surface precipitation (cf. Figure 12a). The temporal change of MPE (i.e., the evolution of hourly MPE in each PPE member related to the synoptic evolution) amounts to 10–15%. The maximum MPE difference between the individual PPE members has the same order of magnitude. For example, during the main WCB ascent phase on October 4, MPE in the unperturbed reference simulation amounts to 35% and decreases to 20% towards the end of the simulation when WCB ascent weakens. This is of similar magnitude to the difference between the CCN end members: the temporal averaged MPE of the high CCN end member amounts to 18%, whereas it amounts to 34% in the low CCN end member (Figure 12b). This illustrates that prescribed aerosol concentrations in this case study can influence the precipitation efficiency similarly strongly as the variability in the synoptic forcing.

We use the temporal mean MPE (discarding the first 3 hr to account for model spin-up; Figure 12b) to train a Gaussian process. Subsequent variance decomposition (Figure 13) suggests that the MPE is most strongly influenced by CCN perturbations with additional uncertainty contributions from ice-phase microphysics (INP and CAP). Although the contribution of INP and CAP to total variance in MPE is smaller than the contribution from CCN, uncertainties related to ice-phase microphysics also influence MPE in the WCB cloud band. Consistent with previous studies (e.g., Barrett & Hoose, 2023; Noppel *et al.*, 2010) on the impact of aerosol concentrations on (convective) clouds, MPE is reduced when CCN concentrations are increased. Enhanced CCN concentrations increase the number concentration of cloud droplets, and thus shift the cloud droplet size distribution to smaller droplet diameters. Consequently, the conversion of cloud droplets to rain is less efficient, as the collision–coalescence process is reduced. This, in turn, increases the cloud liquid water path (Supporting Information Figure A7a), and thus the total water path (Figure 12c). In summary, CCN concentrations substantially influence precipitation efficiency and detailed WCB cloud structure, such as the total water path, whereas SST perturbations determine total surface precipitation sums through their control on specific humidity influx into the system.

Those two different impacts also arise in the Lagrangian perspective. Considering the LPE, two different aspects need to be considered (Figure 12d). Prior to the start of WCB ascent at $t = 0$ hr (defined as the start time of the fastest 600 hPa ascent period), LPE is large and approaches 1 (Figure 12d). This is caused by precipitation that sediments from above into the WCB air parcels that are still located in the lower troposphere prior to their ascent. Air parcels are mostly located below the cloud base; that is, cloud droplets are mostly absent and cloud formation through cloud droplet activation and subsequent condensational growth is not yet active. Thus, prior to the ascent, the WCB air parcel's hydrometeor content is substantially influenced by the precipitating cloud from above (Figure 12d). In this phase, the major source of uncertainty is related to SST perturbations (Figures 12d and 13), as the total precipitation, which is related to q_r near the surface, is strongly influenced by SST (as discussed earlier herein). After the start of the ascent at $t = 0$ hr, cloud formation through cloud droplet activation and subsequent condensational growth of cloud droplets starts along the WCB trajectories in all PPE members. Thus, q_c increases, leading to a decrease of LPE following the ascent (Figure 12d). Depending on the precipitation efficiency, a fraction of the newly formed q_c is converted to q_r. The more efficiently that q_c is converted into q_r, the larger the LPE remains along the ascent. In general, LPE decreases continuously along the ascent, because at colder temperature the ice-phase processes dominate, and ice, snow, and graupel become more relevant, which is not accounted for in this definition of LPE. After the start of the ascent, the major influence on LPE results from the representation of CCN. Consistent with MPE, larger CCN concentrations substantially reduce the conversion efficiency of cloud droplets to raindrops, which leads to a continuously lower LPE along the ascent (Figure 12d).

To quantify the contribution of individual parameters to the described variance in LPE evolution, we train Gaussian processes for LPE at characteristic time steps. These times include the time of maximum LPE prior to the start of the ascent ($\mathrm{LPE}_\mathrm{max}$; Figure 12d) and 5 hr after the ascent (LPE_5h) when the liquid fraction

is still large. As described qualitatively earlier herein, variance-based sensitivity analysis confirms that the major source of uncertainty for maximum LPE before ascent is SST (Figure 13), which mainly influences the total rainwater content through enhanced ascent and moisture availability. The contribution of SST to the variance in LPE is reduced during the ascent and is reduced to almost 0% during the ascent at $t = 5$ hr and afterwards. At that time, CCN have the largest main effect and are thus the dominant source of uncertainty for LPE. Yet, the main effect of CCN also decreases along the ascent at later times, and the contribution from the interaction terms between the individual parameters increases (not shown). At colder temperatures, ice-phase microphysical processes become more active and interact with the warm-phase microphysical processes in the mixed-phase region. The increasing contribution from the parameter interactions may suggest that complicated process interactions become more important in the mixed-phase region. More in-depth analysis of individual process rates that determine the detailed cloud structure and precipitation formation in the ice-phase and mixed-phase is required to understand such process interactions, which is beyond the scope of this study.

In the following, we illustrate how combined changes in precipitation efficiency and total precipitation sums influence surface precipitation distribution and intensity.

5.3 | Precipitation distribution and intensity

To illustrate how changes in precipitation efficiency influence the spatial precipitation distribution and intensity, we compute surface precipitation composites for each ensemble member (Figure 14a). To account for the variability and spatial shifts of the WCB inflow region (see Figure 7), the composites are centred relative to the centre of mass of the poleward-shifting WCB inflow region and are averaged over the first 2 days of the simulation (afterwards the WCB inflow region is less well confined due to the very small number of WCB trajectories). Specifically, we focus on the impact of CCN concentration as the primary influence on precipitation efficiency results from CCN perturbations (Figure 13).

The precipitation composite for the unperturbed reference simulation (Figure 14a, black contours) illustrates the southwest to northeast extended precipitating WCB cloud band (Figure 1a,c,e). The precipitation rates are strongest in an elongated band around the average WCB inflow region ahead of the cold front (Figures 1a,c,e, and 14a). To illustrate the effect of CCN concentrations on the surface precipitation distribution, the difference between composites of the low and high CCN end members is shown (Figure 14a); that is, green shading shows where the low CCN end member produces higher surface precipitation rates, and brown shading shows where the high CCN end member has higher precipitation rates. Though the area mean composite precipitation hardly differs between the low and high CCN concentration simulations, as expected from the relatively small effect of CCN on total precipitation sums (Figure 13), a dipole structure is visible. The low CCN simulation is characterised by higher precipitation rates in the main precipitating region near the mean WCB inflow region. In contrast, in the high CCN simulation, the precipitation rates are larger further to the east; that is, downstream of the mean WCB inflow region considering the eastward movement of the entire system. The downstream shift of surface precipitation relative to the WCB is consistent with a delayed precipitation formation for high CCN concentrations, whereas in cleaner conditions precipitation formation is more efficient and the cloud precipitates more readily. At the downstream side of the cloud band the reduction in precipitation for low CCN conditions amounts to 80–100% of precipitation in the unperturbed reference (Figure 14b, purple shading). In contrast, in the core precipitating region, the precipitation difference between the low and high CCN members exceeds 30% of precipitation in the unperturbed reference simulation (Figure 14b, green shading).

Hence, in addition to a downstream shift of the precipitating region, high CCN concentrations also reduce the precipitation intensity in the cold frontal region of the WCB (Figure 14b,c). Indeed, the frequency of the most intense hourly surface precipitation rates in high CCN conditions is reduced compared with low CCN conditions (Figure 14c). Figure 14d shows the ratios of binned surface precipitation rate frequencies for selected subgroups of the PPE (see Figure 14c for distributions of hourly precipitation rate frequencies across the PPE). For each subgroup, the PPE is split in half stratified by the respective perturbed parameter values. For example, the green curve shows the ratio of low CCN to high CCN PPE members, and suggests that the most intense surface precipitation rates more frequently occur in low CCN members. In contrast, the frequency of less intense precipitation rates is reduced in low CCN members. SST perturbations (red curve in Figure 14d) also influence the precipitation rate distributions: higher SST conditions are consistently associated with a higher frequency of precipitation in all intensity ranges. Generally, for moderate precipitation rates, SST seems to dominate the impact, whereas for the most intense precipitation rates the CCN seem to be the dominant influence.

To corroborate the parameter influence on precipitation intensity we emulate the frequency of the most intense precipitation rates, defined as exceedance of the 99.9th

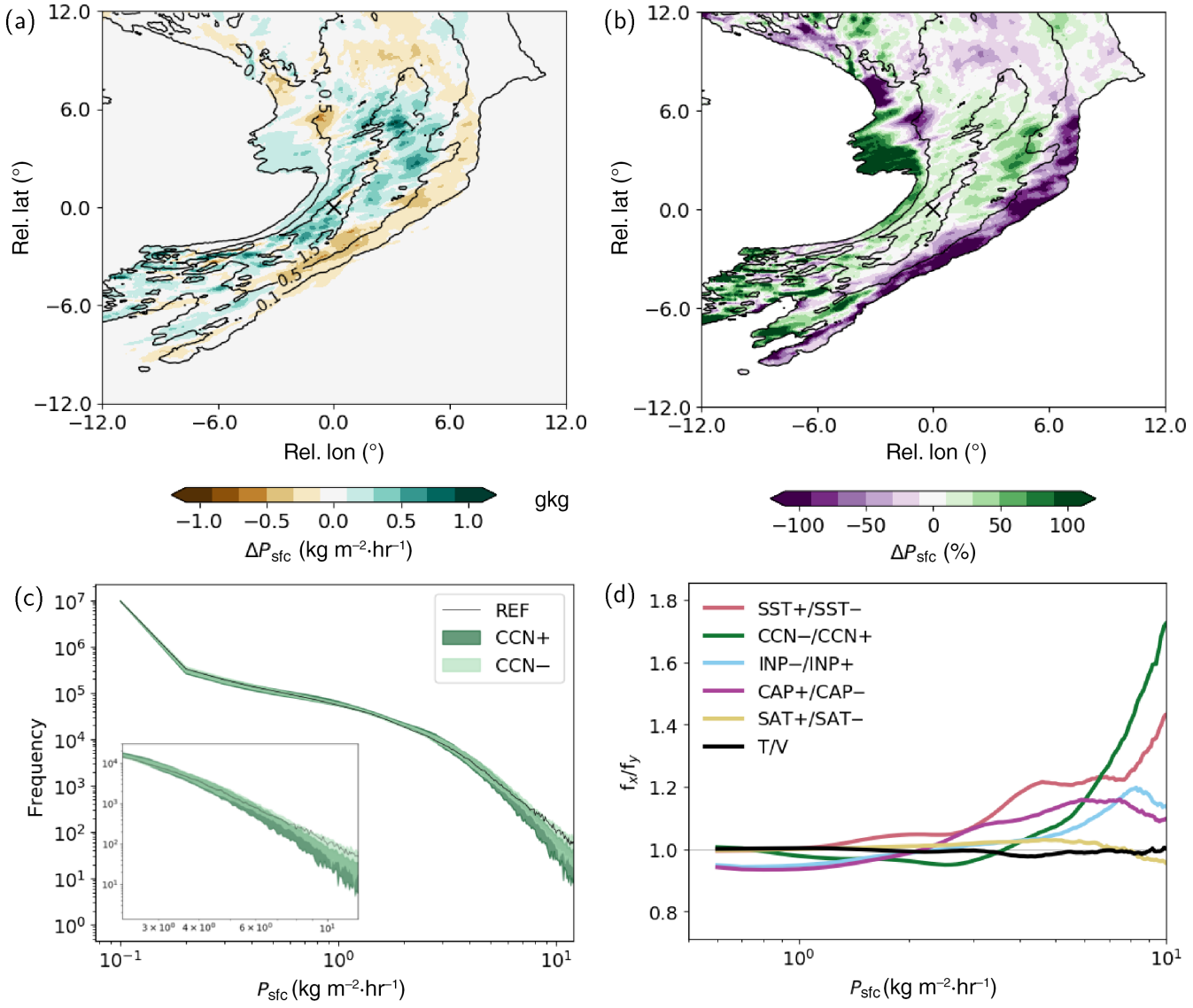

FIGURE 14 (a) Warm conveyor belt (WCB) inflow centred composites of surface precipitation. Black contours show composite precipitation centred relative to average WCB trajectory inflow position for the reference simulation at 0.1, 0.5 and 1.5 kg · m^{-2}. Shading shows the composite difference between the end member simulations with high and low cloud concentration nuclei (CCN) concentrations (CCN − −CCN+); that is, green colours indicate enhanced surface precipitation in CCN− and brown colours indicate enhanced surface precipitation in CCN+. (b) As (a) but the difference between CCN− and CCN+ is shown relative to the unperturbed reference simulation: (CCN − −CCN+)/REF (%). (c) Histogram of hourly surface precipitation rates (kg · m^2 · hr^{-1}) for the unperturbed reference simulation (REF) and the envelopes for perturbed parameter ensemble (PPE) members with high and low CCN concentrations, respectively, for a bin width of 0.1 mm · hr^{-1}. (d) Ratios of binned surface precipitation rate frequencies for selected subgroups of the PPE x and y (f_x/f_y). Shown are ratios of low and high CCN members (green), high and low sea-surface temperature (SST; red), low and high ice nucleating particle concentration (INP; blue), high and low capacitance (CAP; purple), and low and high supersaturation (SAT; orange). Additionally, the ratio of training and validation data is shown as reference (T/V).

percentile of hourly precipitation rates in the unperturbed reference simulation. Variance decomposition shows that CCN have a dominant impact on the precipitation intensity, with additional contributions from SST. Specifically, low CCN concentrations and high SST result in higher precipitation intensity (Figure 13).

To summarise, the influence of SST on WCB inflow specific humidity and WCB ascent most strongly influences total domain-integrated surface precipitation at longer lead times. The precipitation efficiency is substantially influenced by cloud microphysical parameters, in particular CCN, but also CAP and INP, and delays

precipitation formation, which subsequently influences surface precipitation sums for shorter integration times of 24–36 hr. The delay of precipitation formation in high CCN conditions also results in a downstream shift of surface precipitation relative to the WCB ascent region. In contrast, the high precipitation efficiency in conditions with low CCN concentrations increases the surface precipitation rates directly ahead of the cold front, which is thus associated with higher local precipitation intensity.

6 | IMPACT ON UPPER LEVEL LARGE-SCALE FLOW

The ensemble spread of Z500 in the PPE grows particularly in regions where the WCB ascends and in the upstream trough–ridge transition region (Figure 4), as illustrated in Section 3. To identify the dominant pattern of variability in the large-scale flow across the PPE and subsequently determine the individual parameter contributions for the observed differences, we perform an empirical orthogonal function (EOF) analysis of geopotential at 300 hPa (Z300) and 500 hPa (Z500) at three selected representative lead times (dt = 24, 48, and 72 hr). The EOF is applied in the North Atlantic region where the WCB ascends and the upper level ridge amplifies using cosine latitude weights. We use a box located between −40 and +50°E and north of 35°N (Figure 15). The box is successively moved ±5° in all directions, and the resulting EOF patterns are averaged over the EOFs from each moving box. We incorporate the sensitivity test for the location of the box to ensure that the outcome remains independent of the specific domain selection. The variability across different boxes is small, and we thus conclude that the results are not very sensitive to the exact extent of the defined region.

For all three lead times, EOF 1 explains about 80% of variance for Z500 and Z300, whereas EOFs 2 and 3 each explain approximately 2–7% of total variance. The spatial pattern of EOF 1 for Z300 shows strong signals in the WCB ascent and upstream trough region at a lead time of 24 hr (Supporting Information Figure A9c) and 48 hr (Figure 15a and Supporting Information Figure A9f), and in the large-scale amplifying ridge at 72 hr (Supporting Information Figure A9i). Figure 15a illustrates a slight westward shift of the upper level ridge after 48 hr lead time for the PPE member that projects the least on the first EOF (red contours; and in blue contours for the PPE member with the strongest projection). The shift of the upstream trough coincides with the WCB trajectory positions (Figure 15b). After 72 hr lead time, the differences in the Z300 pattern between PPE members with the strongest and weakest projection (Supporting Information Figure A9i) emphasise the strength of the upper level ridge and its westward extension; that is, PPE members that weakly project on EOF 1 are characterised by a more westward extended and stronger ridge. Simultaneously, the ridge's eastward extension is reduced (Supporting Information Figure A9i).

The spatial patterns of EOFs 2 and 3 are less coherent and explainable, but also emphasise variance in the detailed upper level ridge characteristics where the WCB ascends (Supporting Information Figures A10 and A11, right columns). The EOF structures of Z500 show patterns similar to those of Z300 (Supporting Information Figures A10 and A11, middle columns) representing variance in the ridge characteristics, and are thus not discussed

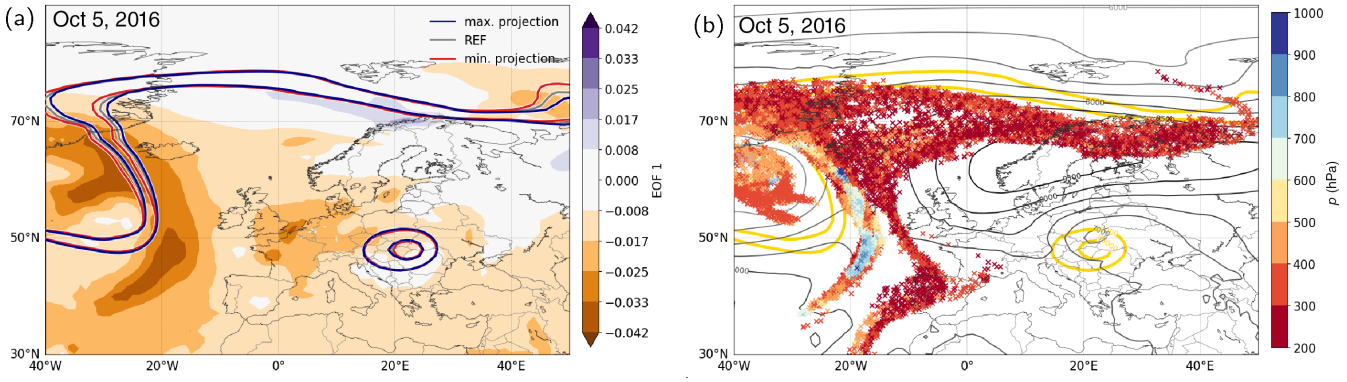

FIGURE 15 (a) Spatial pattern of the first empirical orthogonal function (EOF) of geopotential at 300 hPa (colours) after 48 hr lead time (1800 UTC, October 5, 2016) and geopotential at 300 hPa (contours at 88×10^3 and 89.1×10^3 $m^2 \cdot s^{-2}$) for the unperturbed reference (yellow), and the experiments with maximum (blue) and minimum (red) projection onto the first EOF. (b) Warm conveyor belt (WCB) trajectory positions coloured according to their pressure p (hPa; only every second WCB trajectory is shown) and geopotential at 925 hPa (grey contours; every 50 geopotential metres) and geopotential at 300 hPa (yellow contours at 88×10^3 and 89×10^3 $m^2 \cdot s^{-2}$) for the unperturbed reference at the same time as (a).

in detail. Overall, this illustrates that the combined perturbations are projected onto the upper level large-scale flow, where they can potentially grow (Baumgart *et al.*, 2019; Zhang *et al.*, 2007).

To determine the contributions of the individual perturbed parameters to the EOF pattern, we compare the parameter values with the respective amplitudes of the principal components (PCs) for all PPE members. For example, the amplitudes of PC 1 quantify how the amplitude of EOF 1 varies across the PPE members. Figure 16 (top row and first column) shows the SST perturbation of each PPE member versus the amplitude of the respective first PC for Z300 for the three lead times (see blue dots for $dt = 48$ hr). The strong negative correlation suggests that PPE members with high SST perturbations project negatively on EOF 1, and vice versa. Together with Figure 15a, this shows that higher SST values are associated with a stronger and more westward-directed upper level ridge amplification, consistent with more pronounced WCB ascent driven by higher SST (Section 4.1). This illustrates that the WCB acts as a communicator between surface and the upper level flow and is capable of projecting perturbations to the jet stream, where they can amplify substantially. The link between SST and upper level ride amplification is consistent with previous studies that have showed that North Atlantic blocking air masses experience local moisture uptake in the western North Atlantic prior to their arrival in the block (Wenta *et al.*, 2024; Yamamoto *et al.*, 2021) and that have indicated a sensitivity of North Atlantic blocking to western North Atlantic SST conditions (Croci-Maspoli & Davies, 2009; Roberts *et al.*, 2020, 2021, 2022; Czaja, 2019; Kwon *et al.*, 2020).

The influence of SST on the amplitude of PC 1 increases with increasing lead time (Figure 16, top row), suggesting that the impact of SST on the upper level ridge is continuous and increases with lead time. Moreover, the amplitudes of PC 1 are not systematically correlated with any other perturbed parameter (Figure 16, top row), suggesting that SST is responsible for the major part of the variance in the geopotential height pattern (within the specified parameter ranges). The correlation patterns for Z500 are very similar and shown in Supporting Information Figure A8.

The dominant influence on the spatial patterns of EOFs 2 and 3 are CCN + INP and CAP respectively (Figure 16). The combination of CCN and INP

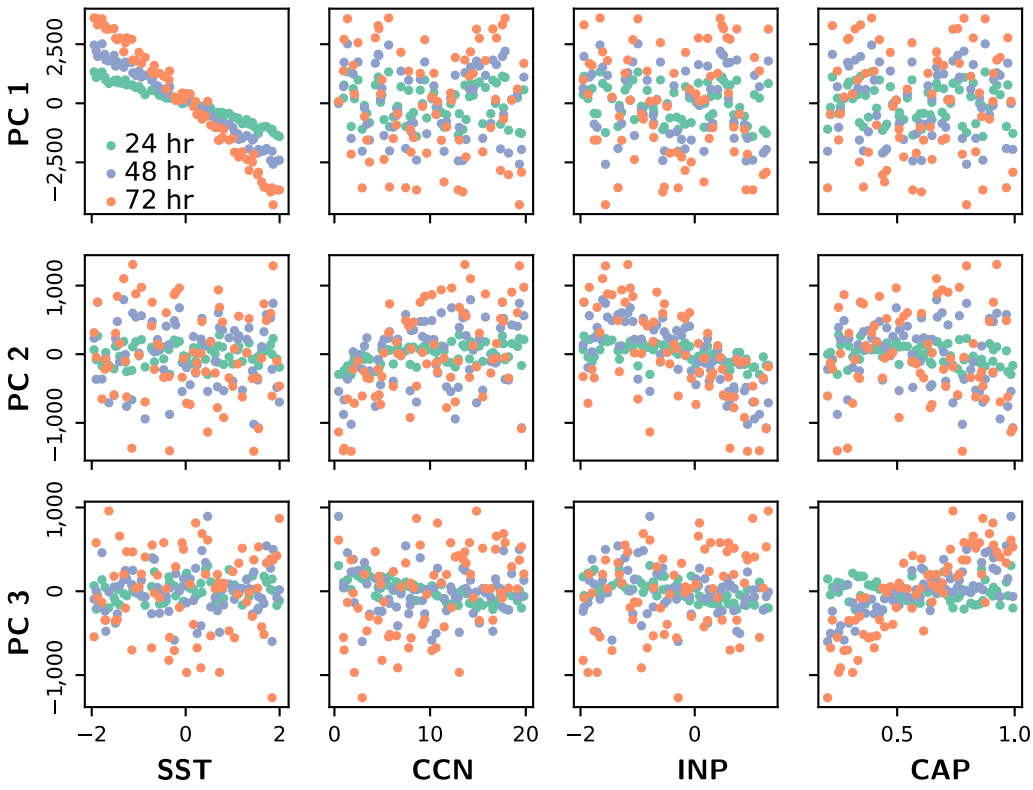

FIGURE 16 Scatter plots of the amplitudes of the first three principal components (PCs) for geopotential at 300 hPa (from top to bottom) versus the parameter perturbations sea-surface temperature (SST), cloud condensation nuclei (CCN), ice nucleating particle concentration (INP), and capacitance (CAP) coloured according to three selected lead times (24 hr, 48 hr, and 72 hr). The results for geopotential at 500 hPa are summarised in Supporting Information Figure A8. We do not include scatter plots for supersaturation (SAT) as no influence of SAT on PC1 to PC3 is visible.

perturbations most strongly influence EOF 2, whereby high CCN and high INP concentrations have an opposing effect. EOF 3 is mostly determined by CAP. This emphasises that the small-scale cloud microphysics perturbations are distinctly imprinted in the characteristics of the upper level ridge, such that the EOF analysis objectively identifies systematic differences. Although the explained variance by the microphysical perturbations is smaller than by SST perturbations, and despite less comprehensive EOF patterns, the small-scale perturbations introduced by cloud microphysical processes are still systematically projected onto the upper level larger-scale flow.

7 | CONCLUDING SUMMARY

The properties of precipitating systems, including the induced modification of the larger scale flow, are influenced by both changes in the larger scale environmental conditions and the details of the microphysics. Here, we investigate the impact of cloud microphysical and environmental condition uncertainty for the large-scale cloud system associated with the WCB airstream. In particular, we adopt a PPE approach combined with Gaussian process emulation to Eulerian and Lagrangian diagnostics and variance-based sensitivity analysis to quantify the influence of parameter perturbations on the WCB ascent, as well as on the associated surface precipitation and the properties of the downstream ridge. The perturbed parameters include CCN and INP concentrations, CAP of ice and snow, equilibrium supersaturation prescribed in the saturation adjustment scheme (SAT), and SST as a proxy for specific humidity and temperature in the WCB inflow region in the lower troposphere. The evolution of the resulting ensemble spread in the PPE from combined cloud microphysical and environmental perturbations is qualitatively similar to a quasi-operational "IFS-SPPT only" configuration (without IC perturbations), indicating that the parameter perturbations reasonably propagate errors to the larger scale flow whereas the individual simulations do not diverge entirely. A quantitative comparison of the different ensembles is limited by the different number of ensemble members used for the calculation of ensemble spread here. In the PPE, the ensemble spread primarily grows where the WCB airstream ascends into the upper level ridge, corroborating the WCB's role in amplifying forecast errors (Grams *et al.*, 2018; Martínez-Alvarado *et al.*, 2016; Pickl *et al.*, 2023).

In summary, we find that SST most strongly influences WCB ascent characteristics, providing a thermodynamic constraint on WCB ascent (Gertler *et al.*, 2023; Joos *et al.*, 2023). Higher SST, and thus increased low-level specific humidity, facilitates more pronounced and faster WCB ascent and is associated with increased air mass transport from the lower into the upper troposphere. On the scale of the WCB airstream, this results in enhanced surface precipitation. Moreover, more pronounced WCB ascent influences the midtropospheric and upper level flow pattern, and is associated with enhanced ridge amplification, leading to a slightly stronger and more westward-extended downstream ridge. This emphasises that the WCB can project low-level perturbations into the mid and upper troposphere near the jet stream, where forecast errors can grow fast (Baumgart *et al.*, 2019).

The cloud microphysical perturbations (specifically CCN, INP, and CAP) have a smaller impact on the large-scale flow. However, EOF analysis also shows that the small-scale microphysical perturbations systematically and distinctly project onto the large-scale flow pattern—albeit to a lesser extent than the SST perturbations. The cloud microphysics impact primarily evolves where the WCB ascends and propagates into the downstream ridge and upstream ridge–trough transition region. Moreover, cloud microphysical perturbations, in particular the prescribed CCN concentration, strongly influence precipitation efficiency, which modulates surface precipitation sums on time-scales of approximately 1 day as well as the local surface precipitation intensity and its spatial distribution. For example, increased aerosol concentrations reduce the precipitation efficiency in the WCB, which leads to a downstream shift of surface precipitation as well as less intense precipitation rates. Overall, the results from this case study suggest that CCN concentrations influence total cloud water path and precipitation efficiency, whereas total surface precipitation sums are constrained by moisture availability, and thus indirectly by SST perturbations. As faster WCB ascent is associated with larger condensate transport into the upper troposphere and lower stratosphere region and a longer lived cirrus cloud shield (Schwenk & Miltenberger, 2024), the sensitivity of WCB ascent behaviour to SST may also influence the upper tropospheric cloud characteristics. Sensitivities of the detailed WCB cloud structure during the ascent and in the outflow region will be explored in further studies. Finally, we find a feedback between cloud microphysical heating and WCB ascent velocity in the mixed- and cold-phase regions. Reduction of the depositional growth rate of ice and snow through lower CAP values leads to a local reduction of vertical velocity in the WCB, as suggested by von Terzi *et al.* (2022) based on observations.

In summary, we show that the combined perturbations influence WCB ascent behaviour and associated precipitation characteristics and are projected onto the larger scale upper level flow through the WCB. Individual uncertain cloud microphysical parameters can influence forecast properties, although their impacts are smaller than

the influence of SST perturbations. Note that the quantification of the dominant sources of uncertainty is only valid within the predefined parameter ranges, and thus depends on the a priori choice of input parameter values. The forecast sensitivity to parameter perturbations presented here is likely model specific and may vary with different parametrisation schemes. In addition, WCB ascent characteristics may be sensitive to additional uncertain model parameters, which could not be tested in this study. Thus, different sensitivities may appear if this approach is extended to additional parameters. We hypothesise that other WCB cases show similar sensitivities. The application of this analysis framework to further WCB cases would show if the sensitivities are more generally valid. Overall, the PPE approach facilitates enhanced process understanding and shows how the WCB airstream propagates forecast errors from the surface into the upper troposphere and from small to larger scales.

ACKNOWLEDGEMENTS

The research leading to these results has been done within the subproject B8 of the Transregional Collaborative Research Center SFB/TRR 165 "Waves to Weather" (www.wavestoweather.de) funded by the German Research Foundation (DFG). CMG is supported by the Helmholtz Association as part of the Young Investigator Group "Sub-seasonal Predictability: Understanding the Role of Diabatic Outflow" (SPREADOUT, grant VH-NG-1243). AO is supported by the Italia–Deutschland science-4-services network in weather and climate (IDEA-S4S; INVACODA, grant no. 4823IDEAP6). This Italian–German research network of universities, research institutes, and the Deutscher Wetterdienst is funded by the BMDV (Federal Ministry of Transport and Digital Infrastructure). We acknowledge support by the state of Baden-Württemberg through bwHPC. The PPE simulations were carried out on the supercomputer HoreKa at Karlsruhe Institute of Technology, Karlsruhe, which is funded by the Ministry of Science, Research and the Arts Baden-Württemberg, Germany, and the German Federal Ministry of Education and Research. Parts of this research were conducted with the supercomputer Mogon II at the Johannes Gutenberg University Mainz, which is a member of the AHRP (Alliance for High-Performance Computing in Rhineland-Palatinate) and the Gauss Alliance e.V. We kindly acknowledge ECMWF and Moritz Pickl for providing the IFS ensemble data for this case study. Open Access funding enabled and organized by Projekt DEAL.

CONFLICT OF INTEREST STATEMENT

The authors declare that they have no conflict of interest.

DATA AVAILABILITY STATEMENT

WCB trajectory data for the 70-member PPE are publicly available in RADAR4KIT https://www.doi.org/10.35097/ecgs4f56mp3ymjmt. Further data that support the findings of this study are available from the corresponding author upon reasonable request.

ORCID

Annika Oertel https://orcid.org/0000-0002-3196-2304
Annette K. Miltenberger https://orcid.org/0000-0003-3320-4272
Christian M. Grams https://orcid.org/0000-0003-3466-9389
Corinna Hoose https://orcid.org/0000-0003-2827-5789

REFERENCES

Barrett, A.I. & Hoose, C. (2023) Microphysical pathways active within thunderstorms and their sensitivity to CCN concentration and wind shear. *Journal of Geophysical Research-Atmospheres*, 128, e2022JD036965.

Barthlott, C. & Hoose, C. (2018) Aerosol effects on clouds and precipitation over Central Europe in different weather regimes. *Journal of the Atmospheric Sciences*, 75, 4247–4264.

Barthlott, C., Zarboo, A., Matsunobu, T. & Keil, C. (2022) Importance of aerosols and shape of the cloud droplet size distribution for convective clouds and precipitation. *Atmospheric Chemistry and Physics*, 22, 2153–2172.

Baumgart, M., Ghinassi, P., Wirth, V., Selz, T., Craig, G.C. & Riemer, M. (2019) Quantitative view on the processes governing the upscale error growth up to the planetary scale using a stochastic convection scheme. *Monthly Weather Review*, 147, 1713–1731.

Bechtold, P., Köhler, M., Jung, T., Doblas-Reyes, F., Leutbecher, M., Rodwell, M.J. et al. (2008) Advances in simulating atmospheric variability with the ECMWF model: from synoptic to decadal time-scales. *Quarterly Journal of the Royal Meteorological Society*, 134, 1337–1351.

Berman, J.D. & Torn, R.D. (2019) The impact of initial condition and warm conveyor belt forecast uncertainty on variability in the downstream waveguide in an ECWMF case study. *Monthly Weather Review*, 147, 4071–4089.

Berman, J.D. & Torn, R.D. (2022) The sensitivity of downstream ridge building forecasts to upstream warm conveyor belt forecast uncertainty using MPAS. *Monthly Weather Review*, 150, 2573–2592.

Bigg, E.K. (1953) The formation of atmospheric ice crystals by the freezing of droplets. *Quarterly Journal of the Royal Meteorological Society*, 79, 510–519.

Binder, H., Boettcher, M., Joos, H. & Wernli, H. (2016) The role of warm conveyor belts for the intensification of extratropical cyclones in northern hemisphere winter. *Journal of the Atmospheric Sciences*, 73, 3997–4020.

Blanchard, N., Pantillon, F., Chaboureau, J.-P. & Delanoë, J. (2020) Organization of convective ascents in a warm conveyor belt. *Weather and Climate Dynamics*, 1, 617–634.

Boettcher, M., Schäfler, A., Sprenger, M., Sodemann, H., Kaufmann, S., Voigt, C. et al. (2021) Lagrangian matches between

observations from aircraft, lidar and radar in a warm conveyor belt crossing orography. *Atmospheric Chemistry and Physics*, 21, 5477–5498.

Boutle, I.A., Belcher, S.E. & Plant, R.S. (2011) Moisture transport in midlatitude cyclones: cyclone Moisture Transport. *Quarterly Journal of the Royal Meteorological Society*, 137, 360–373.

Buizza, R., Leutbecher, M. & Isaksen, L. (2008) Potential use of an ensemble of analyses in the ECMWF ensemble prediction system. *Quarterly Journal of the Royal Meteorological Society*, 134, 2051–2066.

Carnell, R. (2024) R package: latin hypercube samples (version 1.2.0). Available from: https://cran.r-project.org/package=lhs

Chiruta, M. & Wang, P.K. (2003) The capacitance of rosette ice crystals. *Journal of the Atmospheric Sciences*, 60, 836–846.

Chiruta, M. & Wang, P.K. (2005) The capacitance of solid and hollow hexagonal ice columns. *Geophysical Research Letters*, 32, L05803.

Choudhary, A. & Voigt, A. (2022) Impact of grid spacing, convective parameterization and cloud microphysics in icon simulations of a warm conveyor belt. *Weather and Climate Dynamics*, 3, 1199–1214.

Christ, S., Wenta, M., Grams, C.M. & Oertel, A. (2025) From sea to sky: understanding the sea surface temperature impact on an atmospheric blocking event using sensitivity experiments with the icosahedral nonhydrostatic (icon) model. *Weather and Climate Dynamics*, 6, 17–42.

Chuang, P., Charlson, R. & Seinfeld, J. (1997) Kinetic limitations on droplet formation in clouds. *Nature*, 390, 594–596.

Crespo, J.A. & Posselt, D.J. (2016) A-train-based case study of stratiform - convective transition within a warm conveyor belt. *Monthly Weather Review*, 144, 2069–2084.

Croci-Maspoli, M. & Davies, H.C. (2009) Key dynamical features of the 2005/06 european winter. *Monthly Weather Review*, 137, 664–678.

Czaja, A., Frankignoul, C., Minobe, S. & Vannière, B. (2019) Simulating the midlatitude atmospheric circulation: what might we gain from high-resolution modeling of air-sea interactions? *Current Climate Change Reports*, 33, 390–406.

Dacre, H.F., Martínez-Alvarado, O. & Mbengue, C.O. (2019) Linking atmospheric rivers and warm conveyor belt airflows. *Journal of Hydrometeorology*, 20, 1183–1196.

Dearden, C., Vaughan, G., Tsai, T. & Chen, J.-P. (2016) Exploring the diabatic role of ice microphysical processes in two North Atlantic summer cyclones. *Monthly Weather Review*, 144, 1249–1272.

DeMott, P.J., Prenni, A.J., Liu, X., Kreidenweis, S.M., Petters, M.D., Twohy, C.H. et al. (2010) Predicting global atmospheric ice nuclei distributions and their impacts on climate. *Proceedings of the National Academy of Sciences*, 107, 11217–11222.

Eckhardt, S., Stohl, A., Wernli, H., James, P., Forster, C. & Spichtinger, N. (2004) A 15-year climatology of warm conveyor belts. *Journal of Climate*, 17, 218–237.

ECMWF. (2016) IFS Documentation CY43R1 - Part IV: physical processes. *ECMWF Report*.

Feingold, G., McComiskey, A., Yamaguchi, T., Johnson, J.S., Carslaw, K.S. & Schmidt, K.S. (2016) New approaches to quantifying aerosol influence on the cloud radiative effect. *Proceedings of the National Academy of Sciences*, 113, 5812–5819.

Forbes, R.M. & Clark, P.A. (2003) Sensitivity of extratropical cyclone mesoscale structure to the parametrization of ice microphysical processes. *Quarterly Journal of the Royal Meteorological Society*, 129, 1123–1148.

Gehring, J., Oertel, A., Vignon, E., Jullien, N., Besic, N. & Berne, A. (2020) Microphysics and dynamics of snowfall associated with a warm conveyor belt over korea. *Atmospheric Chemistry and Physics*, 20, 7373–7392.

Genz, C., Schrödner, R., Heinold, B., Henning, S., Baars, H., Spindler, G. et al. (2020) Estimation of cloud condensation nuclei number concentrations and comparison to in situ and lidar observations during the hope experiments. *Atmospheric Chemistry and Physics*, 20, 8787–8806.

Gertler, C.G., O'Gorman, P.A. & Pfahl, S. (2023) Moist available potential energy of the mean state of the atmosphere and the thermodynamic potential for warm conveyor belts and convection. *Weather and Climate Dynamics*, 4, 361–379.

Glassmeier, F., Hoffmann, F., Johnson, J.S., Yamaguchi, T., Carslaw, K.S. & Feingold, G. (2019) An emulator approach to stratocumulus susceptibility. *Atmospheric Chemistry and Physics*, 19, 10191–10203.

Grams, C.M. & Archambault, H.M. (2016) The key role of diabatic outflow in amplifying the midlatitude flow: a representative case study of weather systems surrounding western North Pacific extratropical transition. *Monthly Weather Review*, 144, 3847– 3869.

Grams, C.M., Magnusson, L. & Madonna, E. (2018) An atmospheric dynamics perspective on the amplification and propagation of forecast error in numerical weather prediction models: a case study. *Quarterly Journal of the Royal Meteorological Society*, 144, 2577–2591.

Hande, L.B. & Hoose, C. (2017) Partitioning the primary ice formation modes in large eddy simulations of mixed-phase clouds. *Atmospheric Chemistry and Physics*, 17, 14105–14118.

Hande, L.B., Engler, C., Hoose, C. & Tegen, I. (2015) Seasonal variability of Saharan desert dust and ice nucleating particles over Europe. *Atmospheric Chemistry and Physics*, 15, 4389–4397.

Hande, L.B., Engler, C., Hoose, C. & Tegen, I. (2016) Parameterizing cloud condensation nuclei concentrations during HOPE. *Atmospheric Chemistry and Physics*, 16, 12059–12079.

Hieronymus, M., Baumgartner, M., Miltenberger, A. & Brinkmann, A. (2022) Algorithmic differentiation for sensitivity analysis in cloud microphysics. *Journal of Advances in Modeling Earth Systems*, 14, e2021MS002849.

Hoffmann, F., Glassmeier, F., Yamaguchi, T. & Feingold, G. (2020) Liquid water path steady states in stratocumulus: insights from process-level emulation and mixed-layer theory. *Journal of the Atmospheric Sciences*, 77, 2203–2215.

Hogan, R.J. & Bozzo, A. (2018) A flexible and efficient radiation scheme for the ECMWF model. *Journal of Advances in Modeling Earth Systems*, 10, 1990–2008.

Hudson, J.G. & Xie, Y. (1999) Vertical distributions of cloud condensation nuclei spectra over the summertime northeast Pacific and Atlantic Oceans. *Journal of Geophysical Research-Atmospheres*, 104, 30219–30229.

Igel, A.L. & Van Den Heever, S.C. (2021) Invigoration or Enervation of Convective Clouds by Aerosols? *Geophysical Research Letters*, 48, e2021GL093804.

Iooss, B., Veiga, S.D., Janon, A. & Pujol, G. (2023) Sensitivity: Global sensitivity analysis of model outputs. *R package version 1.29.0*, Consortium for Small-Scale Modelling. Available from: https://cran.r-project.org/web/packages/sensitivity/sensitivity.pdf. [Accessed 09 2023]

Johnson, J.S., Cui, Z., Lee, L.A., Gosling, J.P., Blyth, A.M. & Carslaw, K.S. (2015) Evaluating uncertainty in convective cloud microphysics using statistical emulation. *Journal of Advances in Modeling Earth Systems*, 7, 162–187.

Joos, H. & Forbes, R.M. (2016) Impact of different IFS microphysics on a warm conveyor belt and the downstream flow evolution. *Quarterly Journal of the Royal Meteorological Society*, 142, 2727–2739.

Joos, H. & Wernli, H. (2012) Influence of microphysical processes on the potential vorticity development in a warm conveyor belt: a case-study with the limited-area model COSMO. *Quarterly Journal of the Royal Meteorological Society*, 138, 407–418.

Joos, H., Madonna, E., Witlox, K., Ferrachat, S., Wernli, H. & Lohmann, U. (2017) Effect of anthropogenic aerosol emissions on precipitation in warm conveyor belts in the western north pacific in winter – a model study with echam6-ham. *Atmospheric Chemistry and Physics*, 17, 6243–6255.

Joos, H., Sprenger, M., Binder, H., Beyerle, U. & Wernli, H. (2023) Warm conveyor belts in present-day and future climate simulations – Part 1: climatology and impacts. *Weather and Climate Dynamics*, 4, 133–155.

Khain, A.P., Beheng, K.D., Heymsfield, A., Korolev, A., Krichak, S.O., Levin, Z. et al. (2015) Representation of microphysical processes in cloud-resolving models: spectral (bin) microphysics versus bulk parameterization. *Reviews of Geophysics*, 53, 247–322.

Korolev, A.V. & Mazin, I.P. (2003) Supersaturation of water vapor in clouds. *Journal of the Atmospheric Sciences*, 60, 2957–2974.

Kwon, Y.-O., Seo, H., Ummenhofer, C.C. & Joyce, T.M. (2020) Impact of multidecadal variability in Atlantic SST on winter atmospheric blocking. *Journal of Climate*, 33, 867–892.

Lebo, Z.J., Morrison, H. & Seinfeld, J.H. (2012) Are simulated aerosol-induced effects on deep convective clouds strongly dependent on saturation adjustment? *Atmospheric Chemistry and Physics*, 12, 9941–9964.

Lee, L.A., Carslaw, K.S., Pringle, K.J., Mann, G.W. & Spracklen, D.V. (2011) Emulation of a complex global aerosol model to quantify sensitivity to uncertain parameters. *Atmospheric Chemistry and Physics*, 11, 12253–12273.

Leutbecher, M. & Palmer, T. (2008) Ensemble forecasting. *Journal of Computational Physics*, 227, 3515–3539 Predicting weather, climate and extreme events.

Leutbecher, M., Lock, S.-J., Ollinaho, P., Lang, S.T.K., Balsamo, G., Bechtold, P. et al. (2017) Stochastic representations of model uncertainties at ECMWF: state of the art and future vision. *Quarterly Journal of the Royal Meteorological Society*, 143, 2315–2339.

Lin, Y. & Colle, B.A. (2011) A new bulk microphysical scheme that includes riming intensity and temperature-dependent ice characteristics. *Monthly Weather Review*, 139, 1013–1035.

Loeppky, J.L., Sacks, J. & Welch, W.J. (2009) Choosing the sample size of a computer experiment: a practical guide. *Technometrics*, 51, 366–376.

Lott, F. & Miller, M.J. (1997) A new subgrid-scale orographic drag parametrization: its formulation and testing. *Quarterly Journal of the Royal Meteorological Society*, 123, 101–127.

Madonna, E., Wernli, H., Joos, H. & Martius, O. (2014) Warm conveyor belts in the ERA-Interim dataset (1979-2010). Part I: climatology and potential vorticity evolution. *Journal of Climate*, 27, 3–26.

Martínez-Alvarado, O., Joos, H., Chagnon, J., Boettcher, M., Gray, S.L., Plant, R.S. et al. (2014) The dichotomous structure of the warm conveyor belt. *Quarterly Journal of the Royal Meteorological Society*, 140, 1809–1824.

Martínez-Alvarado, O., Madonna, E., Gray, S.L. & Joos, H. (2016) A route to systematic error in forecasts of Rossby waves. *Quarterly Journal of the Royal Meteorological Society*, 142, 196–210.

Mazoyer, M., Ricard, D., Rivière, G., Delanoë, J., Arbogast, P., Vié, B. et al. (2021) Microphysics impacts on the warm conveyor belt and ridge building of the NAWDEX IOP6 cyclone. *Monthly Weather Review*, 149, 3961–3980.

Mazoyer, M., Ricard, D., Rivière, G., Delanoö, J., Riette, S., Augros, C. et al. (2023) Impact of mixed-phase cloud parameterization on warm conveyor belts and upper-tropospheric dynamics. *Monthly Weather Review*, 151, 1073–1091.

McCoy, D.T., Field, P.R., Schmidt, A., Grosvenor, D.P., Bender, F.A.-M., Shipway, B.J. et al. (2018) Aerosol midlatitude cyclone indirect effects in observations and high-resolution simulations. *Atmospheric Chemistry and Physics*, 18, 5821–5846.

Miltenberger, A.K., Reynolds, S. & Sprenger, M. (2016) Revisiting the latent heating contribution to foehn warming: Lagrangian analysis of two foehn events over the Swiss Alps. *Quarterly Journal of the Royal Meteorological Society*, 142, 2194–2204.

Miltenberger, A.K., Lüttmer, T. & Siewert, C. (2020) Secondary ice formation in idealised deep convection - source of primary ice and impact on glaciation. *Atmosphere*, 11, 542.

Morris, M.D. & Mitchell, T.J. (1995) Exploratory designs for computational experiments. *Journal of Statistical Planning and Inference*, 43, 381–402.

Morrison, H. & Grabowski, W.W. (2008) Modeling supersaturation and subgrid-scale mixing with two-moment bulk warm microphysics. *Journal of the Atmospheric Sciences*, 65, 792–812.

Neuhauser, C., Hieronymus, M., Kern, M., Rautenhaus, M., Oertel, A. & Westermann, R. (2023) Visual analysis of model parameter sensitivities along warm conveyor belt trajectories using Met.3D (1.6.0-multivar0). *Geoscientific Model Development*, 16, 4617–4638.

Noppel, H., Blahak, U., Seifert, A. & Beheng, K.D. (2010) Simulations of a hailstorm and the impact of CCN using an advanced two-moment cloud microphysical scheme. *Atmospheric Research*, 96, 286–301.

O'Hagan, A. (2006) Bayesian analysis of computer code outputs: a tutorial. *Reliability Engineering & System Safety*, 91, 1290–1300 The Fourth International Conference on Sensitivity Analysis of Model Output (SAMO 2004).

Oakley, J.E. & O'Hagan, A. (2004) Probabilistic sensitivity analysis of complex models: a bayesian approach. *Journal of the Royal Statistical Society Series B: Statistical Methodology*, 66, 751–769.

Oertel, A., Boettcher, M., Joos, H., Sprenger, M., Konow, H., Hagen, M. et al. (2019) Convective activity in an extratropical cyclone and its warm conveyor belt - a case-study combining observations and a convection-permitting model simulation. *Quarterly Journal of the Royal Meteorological Society*, 145, 1406–1426.

Oertel, A., Boettcher, M., Joos, H., Sprenger, M. & Wernli, H. (2020) Potential vorticity structure of embedded convection in a warm conveyor belt and its relevance for large-scale dynamics. *Weather and Climate Dynamics*, 1, 127–153.

Oertel, A., Sprenger, M., Joos, H., Boettcher, M., Konow, H., Hagen, M. et al. (2021) Observations and simulation of intense convection embedded in a warm conveyor belt – how ambient vertical wind shear determines the dynamical impact. *Weather and Climate Dynamics*, 2, 89–110.

Oertel, A., Miltenberger, A.K., Grams, C.M. & Hoose, C. (2023a) Interaction of microphysics and dynamics in a warm conveyor belt simulated with the icosahedral nonhydrostatic (icon) model. *Atmospheric Chemistry and Physics*, 23, 8553–8581.

Oertel, A., Pickl, M., Quinting, J.F., Hauser, S., Wandel, J., Magnusson, L. et al. (2023b) Everything hits at once: how remote rainfall matters for the prediction of the 2021 North American heat wave. *Geophysical Research Letters*, 50, e2022GL100958.

Orr, A., Bechtold, P., Scinocca, J., Ern, M. & Janiskova, M. (2010) Improved middle atmosphere climate and forecasts in the ECMWF model through a nonorographic gravity wave drag parameterization. *Journal of Climate*, 23, 5905–5926.

Pfahl, S., Madonna, E., Boettcher, M., Joos, H. & Wernli, H. (2014) Warm conveyor belts in the ERA-Interim data set (1979-2010). Part II: moisture origin and relevance for precipitation. *Journal of Climate*, 27, 27–40.

Pickl, M., Lang, S.T.K., Leutbecher, M. & Grams, C.M. (2022) The effect of stochastically perturbed parametrisation tendencies (sppt) on rapidly ascending air streams. *Quarterly Journal of the Royal Meteorological Society*, 148, 1242–1261.

Pickl, M., Quinting, J.F. & Grams, C.M. (2023) Warm conveyor belts as amplifiers of forecast uncertainty. *Quarterly Journal of the Royal Meteorological Society*, 149, 3064–3085.

Pomroy, H.R. & Thorpe, A.J. (2000) The evolution and dynamical role of reduced upper-tropospheric potential vorticity in intensive observing period one of FASTEX. *Monthly Weather Review*, 128, 1817–1834.

Posselt, D.J., Fryxell, B., Molod, A. & Williams, B. (2016) Quantitative sensitivity analysis of physical parameterizations for cases of deep convection in the NASA GEOS-5. *Journal of Climate*, 29, 455–479.

Quinting, J.F. & Grams, C.M. (2021) Toward a systematic evaluation of warm conveyor belts in numerical weather prediction and climate models. Part I: predictor selection and logistic regression model. *Atmospheric Sciences*, 78, 1465–1485.

Quinting, J.F. & Grams, C.M. (2022) EuLerian identification of ascending AirStreams (ELIAS 2.0) in numerical weather prediction and climate models - Part 1: development of deep learning model. *Geoscientific Model Development*, 15, 715–730.

Raschendorfer, M. (2018) *The new turbulence parameterization of LM. Cosmo news letter no. 1, Consortium for Small-Scale Modelling*. Offenbach am Main, Germany: Deutscher Wetterdienst. Available from: http://www.cosmo-model.org/content/model/documentation/newsLetters/newsLetter01/newsLetter_01.pdf. [Accessed 12 2021]

Rasmussen, C.E. (2004) *Gaussian Processes in machine learning*. Berlin, Heidelberg: Springer Berlin Heidelberg, pp. 63–71. Available from: https://doi.org/10.1007/978-3-540-28650-9_4

Rasmussen, C.E. & Williams, C.K.I. (2006) *Gaussian processes for machine learning*. London: MIT Press.

Rasp, S., Selz, T. & Craig, G. (2016) Convective and slantwise trajectory ascent in convection-permitting simulations of midlatitude cyclones. *Monthly Weather Review*, 144, 3961–3976.

Riemer, M. & Jones, S.C. (2010) The downstream impact of tropical cyclones on a developing baroclinic wave in idealized scenarios of extratropical transition. *Quarterly Journal of the Royal Meteorological Society*, 136, 617–637.

Rivière, G., Wimmer, M., Arbogast, P., Piriou, J.-M., Delanoë, J., Labadie, C. et al. (2021) The impact of deep convection representation in a global atmospheric model on the warm conveyor belt and jet stream during NAWDEX IOP6. *Weather and Climate Dynamics*, 2, 1011–1031.

Roberts, C.D., Vitart, F., Balmaseda, M.A. & Molteni, F. (2020) The time-scale-dependent response of the wintertime north Atlantic to increased ocean model resolution in a coupled forecast model. *Journal of Climate*, 33, 3663–3689.

Roberts, C.D., Vitart, F. & Balmaseda, M.A. (2021) Hemispheric impact of north Atlantic SSTS in subseasonal forecasts. *Geophysical Research Letters*, 48, e2020GL0911446.

Roberts, C.D., Balmaseda, M.A., Tietsche, S. & Vitart, F. (2022) Sensitivity of ECMWF coupled forecasts to improved initialization of the ocean mesoscale. *Quarterly Journal of the Royal Meteorological Society*, 148, 3694–3714.

Rodwell, M., Forbes, R. & Wernli, H. (2017) Why warm conveyor belts matter in NWP. *ECMWF Newsletter*, 154, 21–28.

Saltelli, A., Tarantola, S. & Chan, K.P.-S. (1999) A quantitative model-independent method for global sensitivity analysis of model output. *Technometrics*, 41, 39–56.

Sánchez, C., Gray, S., Volonté, A., Pantillon, F., Berthou, S. & Davolio, S. (2024) The impact of preceding convection on the development of medicane ianos and the sensitivity to sea surface temperature. *Weather and Climate Dynamics*, 5, 1429–1455.

Schäfler, A. & Harnisch, F. (2015) Impact of the inflow moisture on the evolution of a warm conveyor belt. *Quarterly Journal of the Royal Meteorological Society*, 141, 299–310.

Schäfler, A., Dörnbrack, A., Wernli, H., Kiemle, C. & Pfahl, S. (2011) Airborne lidar observations in the inflow region of a warm conveyor belt. *Quarterly Journal of the Royal Meteorological Society*, 137, 1257–1272.

Schäfler, A., Craig, C., Wernli, H., Arbogast, P., Doyle, J.D., McTaggart-Cowan, R. et al. (2018) The North Atlantic waveguide and downstream impact experiment. *Bulletin of the American Meteorological Society*, 99, 1607–1637.

Schemm, S. (2023) Toward eliminating the decades-old "too zonal and too equatorward" storm-track bias in climate models. *Journal of Advances in Modeling Earth Systems*, 15, e2022MS003482.

Schrom, R.S. & Kumjian, M.R. (2016) Connecting microphysical processes in colorado winter storms with vertical profiles of radar observations. *Journal of Applied Meteorology and Climatology*, 55, 1771–1787.

Schwenk, C. & Miltenberger, A. (2024) The role of ascent timescales for warm conveyor belt (WCB) moisture transport into the upper troposphere and lower stratosphere (UTLS). *Atmospheric Chemistry and Physics*, 24, 14073–14099.

Seifert, A. & Beheng, K. (2006a) A two-moment cloud microphysics parameterization for mixed-phase clouds. Part 1: model description. *Meteorology and Atmospheric Physics*, 92, 45–66.

Seifert, A. & Beheng, K. (2006b) A two-moment cloud microphysics parameterization for mixed-phase clouds. Part 2: maritime vs. continental deep convective storms. *Meteorology and Atmospheric Physics*, 92, 67–82.

Sprenger, M. & Wernli, H. (2015) The LAGRANTO Lagrangian analysis tool – version 2.0. *Geoscientific Model Development*, 8, 2569–2586.

Stein, M. (1987) Large sample properties of simulations using Latin hypercube sampling. *Technometrics*, 29, 143–151.

Steinfeld, D. & Pfahl, S. (2019) The role of latent heating in atmospheric blocking dynamics: a global climatology. *Climate Dynamics*, 53, 6159–6180.

Storelvmo, T. & Tan, I. (2015) The Wegener-Bergeron-Findeisen process - Its discovery and vital importance for weather and climate. *Meteorologische Zeitschrift*, 24, 455–461.

Sui, C.-H., Li, X. & Yang, M.-J. (2007) On the definition of precipitation efficiency. *Journal of the Atmospheric Sciences*, 64, 4506–4513.

von Terzi, L., Dias Neto, J., Ori, D., Myagkov, A. & Kneifel, S. (2022) Ice microphysical processes in the dendritic growth layer: a statistical analysis combining multi-frequency and polarimetric doppler cloud radar observations. *Atmospheric Chemistry and Physics*, 22, 11795–11821.

Teubler, F. & Riemer, M. (2021) Potential-vorticity dynamics of troughs and ridges within rossby wave packets during a 40-year reanalysis period. *Weather and Climate Dynamics*, 2, 535–559.

Tiedtke, M. (1989) A comprehensive mass flux scheme for cumulus parameterization in large-scale models. *Monthly Weather Review*, 117, 1779–1800.

Wang, Y., Zheng, G., Jensen, M.P., Knopf, D.A., Laskin, A., Matthews, A.A. et al. (2021) Vertical profiles of trace gas and aerosol properties over the eastern North Atlantic: variations with season and synoptic condition. *Atmospheric Chemistry and Physics*, 21, 11079–11098.

Watson-Parris, D., Schutgens, N., Reddington, C., Pringle, K.J., Liu, D., Allan, J.D. et al. (2019) In situ constraints on the vertical distribution of global aerosol. *Atmospheric Chemistry and Physics*, 19, 11765–11790.

Wellmann, C., Barrett, A.I., Johnson, J.S., Kunz, M., Vogel, B., Carslaw, K.S. et al. (2018) Using emulators to understand the sensitivity of deep convective clouds and hail to environmental conditions. *Journal of Advances in Modeling Earth Systems*, 10, 3103–3122.

Wellmann, C., Barrett, A.I., Johnson, J.S., Kunz, M., Vogel, B., Carslaw, K.S. et al. (2020) Comparing the impact of environmental conditions and microphysics on the forecast uncertainty of deep convective clouds and hail. *Atmospheric Chemistry and Physics*, 20, 2201–2219.

Wenta, M., Grams, C.M., Papritz, L. & Federer, M. (2024) Linking Gulf Stream air–sea interactions to the exceptional blocking episode in February 2019: a Lagrangian perspective. *Weather and Climate Dynamics*, 5, 181–209.

Wernli, H. & Davies, H.C. (1997) A Lagrangian-based analysis of extratropical cyclones. I: the method and some applications. *Quarterly Journal of the Royal Meteorological Society*, 123, 467–489.

Westbrook, C.D. & Heymsfield, A.J. (2011) Ice crystals growing from vapor in supercooled clouds between -2.5° and $-22^{\circ}C$: testing current parameterization methods using laboratory data. *Journal of the Atmospheric Sciences*, 68, 2416–2429.

Westbrook, C.D., Hogan, R.J. & Illingworth, A.J. (2008) The capacitance of pristine ice crystals and aggregate snowflakes. *Journal of the Atmospheric Sciences*, 65, 206–219.

Wimmer, M., Rivière, G., Arbogast, P., Piriou, J.-M., Delanoë, J., Labadie, C. et al. (2022) Diabatic processes modulating the vertical structure of the jet stream above the cold front of an extratropical cyclone: sensitivity to deep convection schemes. *Weather and Climate Dynamics*, 3, 863–882.

Wylie, D.P. & Hudson, J.G. (2002) Effects of long-range transport and clouds on cloud condensation nuclei in the springtime arctic. *Journal of Geophysical Research-Atmospheres*, 107, AAC 13–1–AAC 13–11.

Yamamoto, A., Nonaka, M., Martineau, P., Yamazaki, A., Kwon, Y.-O., Nakamura, H. et al. (2021) Oceanic moisture sources contributing to wintertime Euro-Atlantic blocking. *Weather and Climate Dynamics*, 2, 819–840.

Zängl, G., Reinert, D., Rípodas, P. & Baldauf, M. (2015) The ICON (ICOsahedral Non-hydrostatic) modelling framework of DWD and MPI-M: description of the non-hydrostatic dynamical core. *Quarterly Journal of the Royal Meteorological Society*, 141, 563–579.

Zängl, G., Reinert, D. & Prill, F. (2022) Grid refinement in ICON v2.6.4. *Geoscientific Model Development*, 15, 7153–7176.

Zhang, F., Bei, N., Rotunno, R., Snyder, C. & Epifanio, C.C. (2007) Mesoscale predictability of moist Baroclinic waves: convection-permitting experiments and multistage error growth dynamics. *Journal of the Atmospheric Sciences*, 64, 3579–3594.

SUPPORTING INFORMATION

Additional supporting information can be found online in the Supporting Information section at the end of this article.

How to cite this article: Oertel, A., Miltenberger, A.K., Grams, C.M. & Hoose, C. (2025) Sensitivities of warm conveyor belt ascent, associated precipitation characteristics and large-scale flow pattern: Insights from a perturbed parameter ensemble. *Quarterly Journal of the Royal Meteorological Society*, e4986. Available from: https://doi.org/10.1002/qj.4986